Insights on the Structure in Solution of Paramagnetic LnIII/GaIII 12-Metallacrown-4 Complexes Using 1D 1H NMR and Model Structures

Insights on the Structure in Solution of Paramagnetic Ln^{III} /Ga^{III} 12-Metallacrown-4 Complexes Using 1D ^{1}H NMR and DFT models

Journal:	*Inorganic Chemistry*
Manuscript ID	ic-2023-00983e
Manuscript Type:	Article
Date Submitted by the Author:	27-Mar-2023
Complete List of Authors:	Melegari, Matteo; Universita degli Studi di Parma, Dipartimento di Scienze Chimiche della Vita e della Sostenibilita Ambientale Marzaroli, Vittoria; Universita degli Studi di Parma, Dipartimento di Scienze Chimiche della Vita e della Sostenibilita Ambientale Polisicchio, Rosy; University of Galway Seletti, Davide; Universita degli Studi di Parma, Dipartimento di Scienze Chimiche della Vita e della Sostenibilita Ambientale Marchiò, Luciano; Universita degli Studi di Parma, Dip. SCVSA (Chemistry Building) Pecoraro, Vincent; University of Michigan, Chemistry Department Tegoni, Matteo; Universita degli Studi di Parma, Department of Chemistry, Life Sciences, and Environmental Sustainability

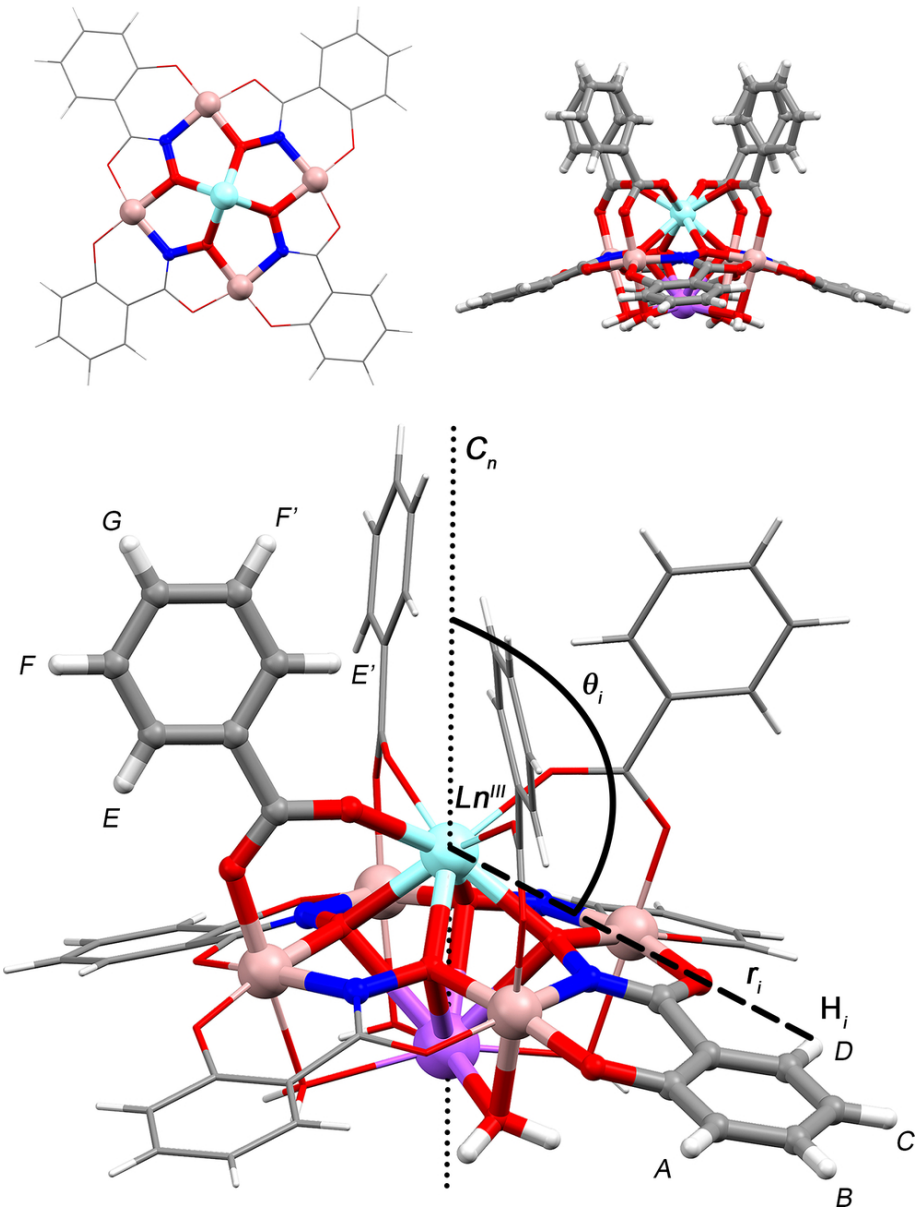

Figure 1. X-ray crystal structure of $Y^{III}Na^{I}(OBz)_4[12\text{-}MC_{GaIII(N)Shi}\text{-}4](H_2O)_4\cdot 6DMF$ complexes (**Y^{III}-1**). Top (upper left) and side views (upper right) of the MC scaffold (benzoate residues were excluded in the top view, disordered Shi^{3-} residues and DMF molecules were omitted for clarity). Lower panel: schematic representation of the geometric parameters r_i and θ_i in **Y^{III}-1** or **Ln^{III}-1** complexes. The principal magnetic axis of the molecule was considered equivalent to the Ln^{III}-Na^{I} direction. Positions labelled with A-F correspond to observable protons in ^{1}H NMR spectra. Cyan: Y^{III}. Brown: Ga^{III}. Purple: Na^{I}.

83x110mm (300 x 300 DPI)

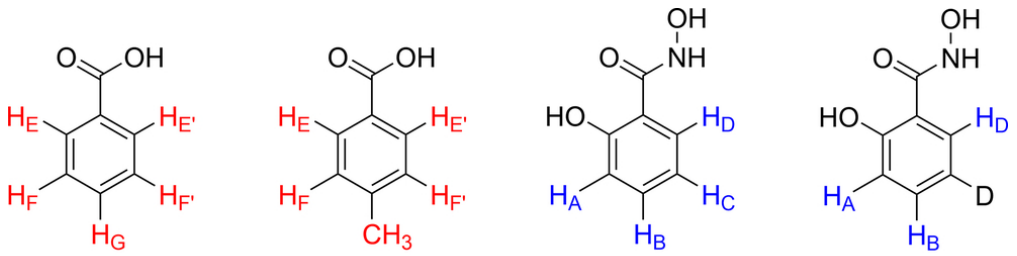

HOBz **HOp-Tol** **H_3Shi** **H_3Shi-d**

Ln^{III}-1 ***Ln^{III}-3*** ***Ln^{III}-1*** ***Ln^{III}-2***

Ln^{III}-2 ***Ln^{III}-3***

Scheme 1. Schematic representation of the ligands (left: BzO^-, right: Shi^{3-}) used in this work. Lettering scheme of protons is reported. The series of complexes for which the ligands are used are reported in italics.

83x38mm (300 x 300 DPI)

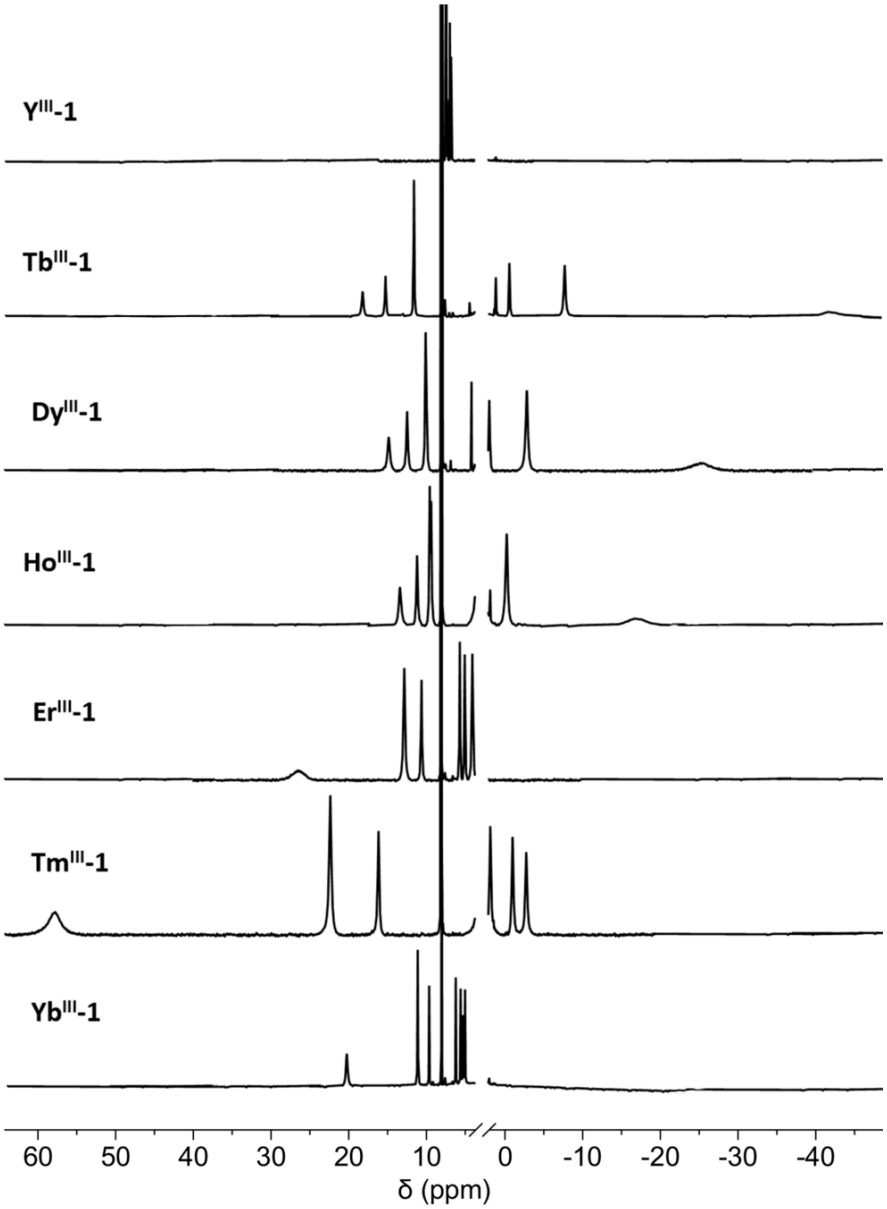

Figure 2. From top to bottom: ^{1}H NMR spectra of **Y^{III}-1**, **Tb^{III}-1**, **Dy^{III}-1**, **Ho^{III}-1**, **Er^{III}-1**, **Tm^{III}-1** and **Yb^{III}-1**. The region 2.00 - 3.50 ppm excluded (solvent signals only).

83x113mm (300 x 300 DPI)

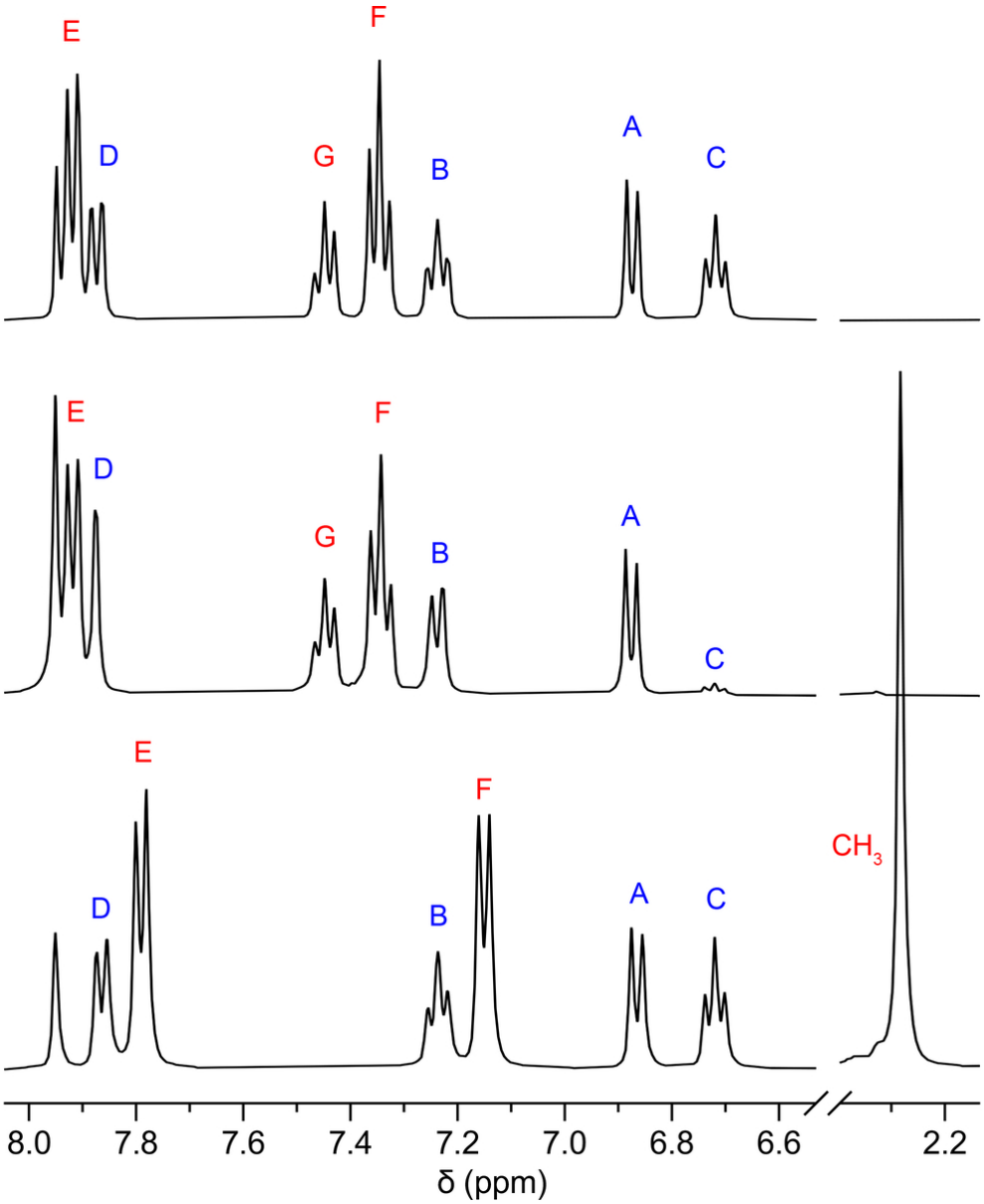

Figure 3. Stacked ^{1}H NMR spectra of $\mathbf{Y^{III}}$**-1**, $\mathbf{Y^{III}}$**-2** and $\mathbf{Y^{III}}$**-3**. Signals are labelled from A to G and the signals of the Shi3- ligands are highlighted in blue, whereas the signals of the BzO^- ligands are highlighted in red, see **Scheme 1**.

83x101mm (300 x 300 DPI)

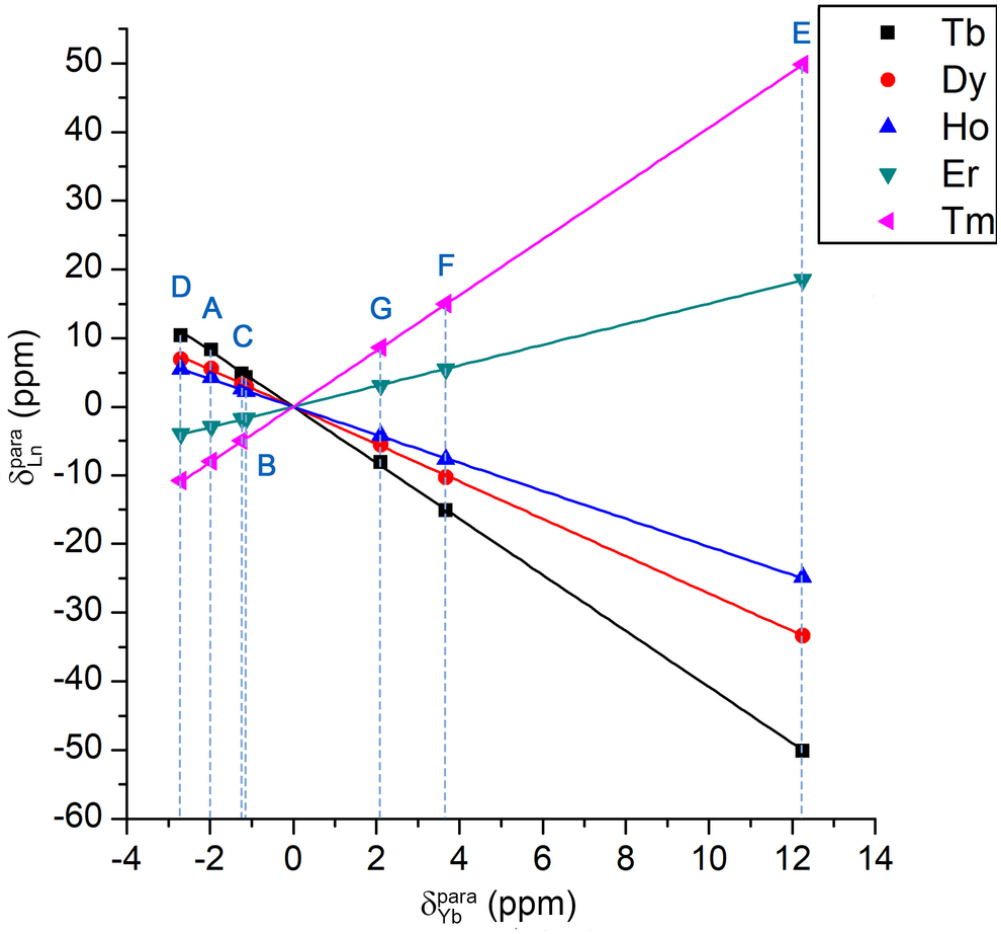

Figure 4. Plot of $\delta_{Ln}^{para}(i)$ as a function of $\delta_{Yb}^{para}(i)$ ("Plot I") for $Ln^{III}Na^{I}(OBz)_4[12\text{-}MC_{GaIII(N)Shi}\text{-}4](H_2O)_4\cdot 6DMF$ (where Ln^{III} = Tb^{III}-Tm^{III}). The A-G labels reported in blue refer to the ligand protons in the corresponding positions.

83x77mm (300 x 300 DPI)

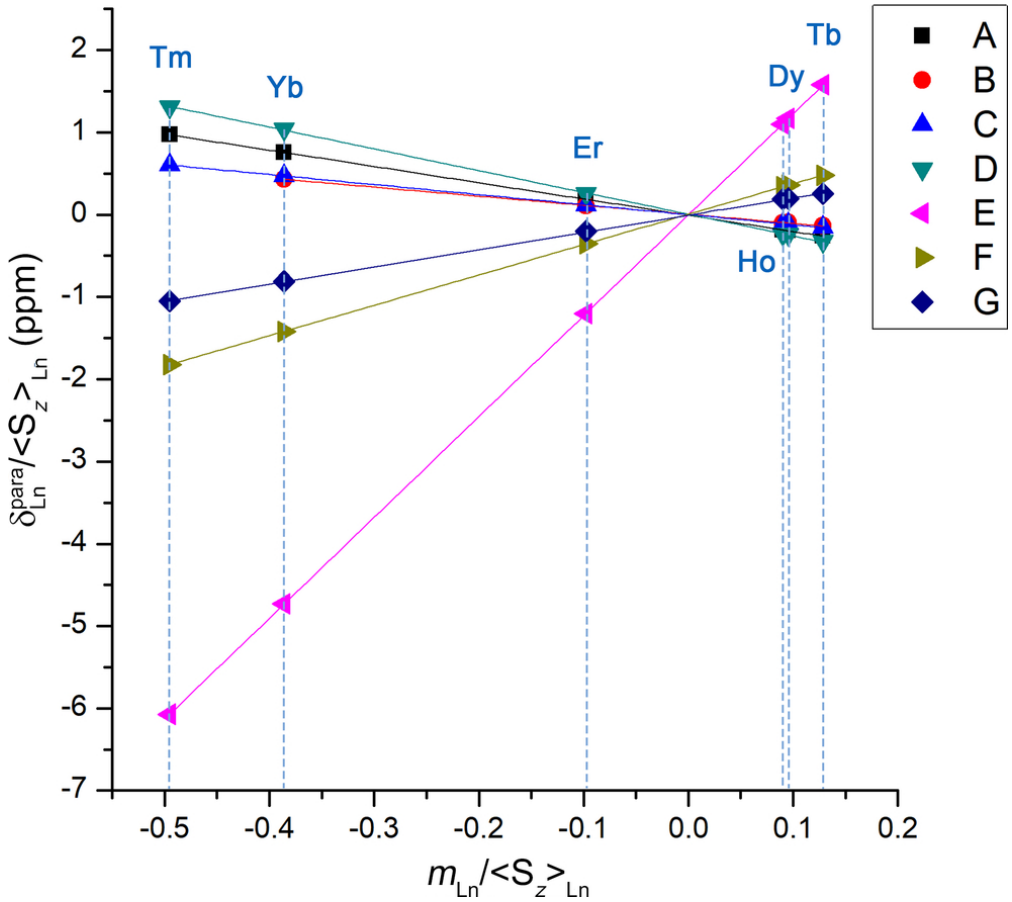

Figure 5. Plot of mLn/$\langle S_z \rangle_{Ln}$ vs δ_{Ln}^{para}(i)/$\langle S_z \rangle_{Ln}$ ("Plot II") for $Ln^{III}Na^{I}(OBz)_4$[12-$MC_{GaIII(N)Shi}$-4]$(H_2O)_4$·6DMF (where Ln^{III} = Tb^{III}-Yb^{III}). Letters correspond to proton positions, while δ_{Ln}^{para} values for each lanthanide are on vertical dashed lines.

83x74mm (300 x 300 DPI)

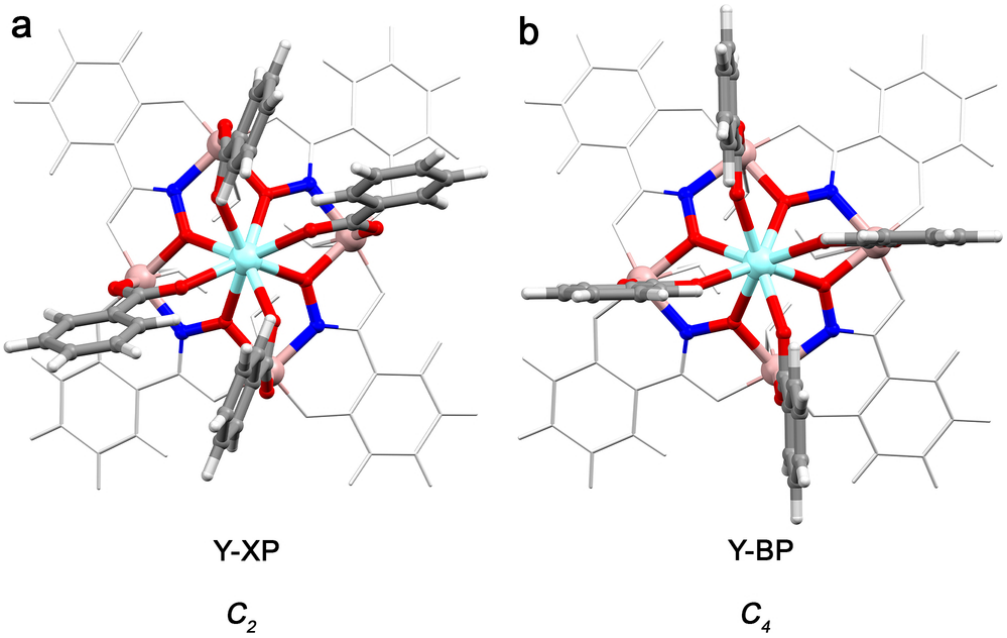

Figure 6. Representation of the conformation of the ligands in the **Y-BP** model (a) and in the **Y-XP** model (b). The structure of **Y-NaBP** is not reported as this model is extremely similar to the **Y-BP** one. The pseudo-symmetry of the models is reported in italics at the bottom. The interactions between the benzoate residues are clearly visible in the pseudo-C_2 model and are however highlighted in the Supporting Information.

83x52mm (300 x 300 DPI)

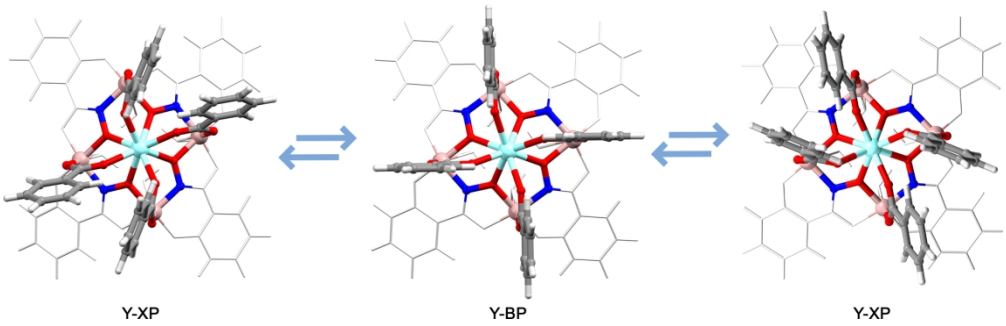

Figure 7. Representation of the fluxionality equilibrium between conformers. On the right the structures **Y-XP** which is pseudo-C_2 symmetrical, at the center the structure **Y-BP** which is pseudo-C_4 symmetrical. The conformer on the right is identical to the one on the left, rotated by 90°.

177x55mm (300 x 300 DPI)

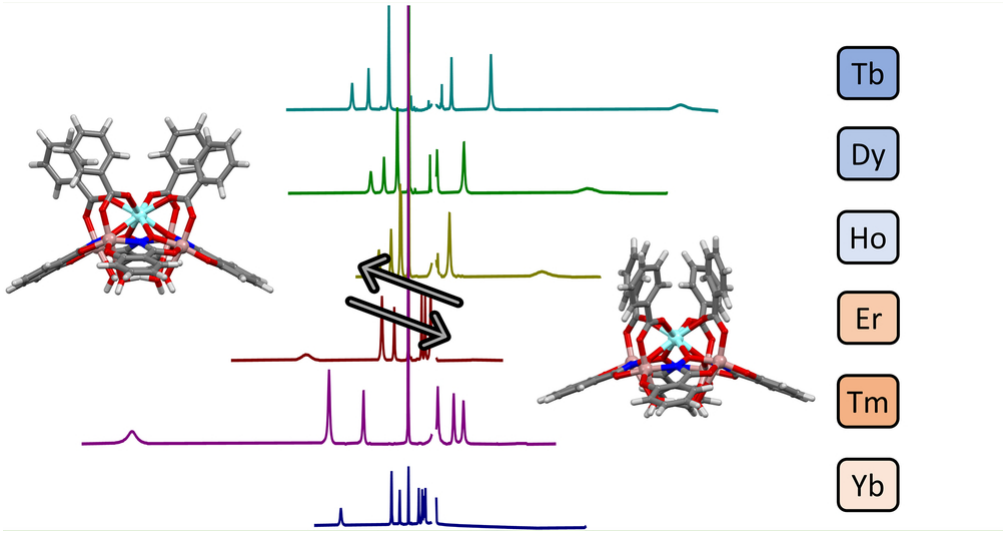

SYNOPSYS The structure in solution of a series of lanthanide metallacrowns were studied through paramagnetic ^{1}H NMR and DFT models. The analysis of NMR data (treated with the "all-lanthanide" method), X-ray structures and DFT models allowed to establish the nature of dynamic equilibrium processes in solution otherwise not noticeable form the X-ray data alone.

84x44mm (300 x 300 DPI)

Insights on the Structure in Solution of Paramagnetic Ln^{III} /Ga^{III} 12-Metallacrown-4 Complexes Using 1D ^{1}H NMR and DFT models

Matteo Melegari, Vittoria Marzaroli, Rosy Polisicchio, Davide Seletti, Luciano Marchiò,

Vincent L. Pecoraro,[†][‡] and Matteo Tegoni*[‡]*

Department of Chemistry, Life Sciences and Environmental Sustainability, University of Parma, Parco Area delle Scienze 17A, 43124 Parma, Italy

[†] Department of Chemistry, Willard H. Dow Laboratories, University of Michigan, Ann Arbor, Michigan 48109, United States

KEYWORDS Metallacrowns • Lanthanide-induced shift • NMR characterization • DFT models • All-lanthanides method.

ABSTRACT The solution structure of $Ln^{III}Na^{I}(OBz)_4$[12-$MC_{GaIII(N)Shi}$-4] complexes were studied through paramagnetic ^{1}H NMR and DFT models. Although nearly isostructural in the solid state, their ^{1}H NMR spectra in DMSO-d_6 are extremely different from one another due to the magnetic anisotropy of the lanthanide(III) ions. NMR data were analyzed by the "all-lanthanide" method that were compared to X-ray structures and DFT models, allowing to establish the extent of the structural changes that occur from the solid state to the solution phase. Major structural changes involve the phenyl groups of the benzoate ions that quite surprisingly do not freely rotate in solution but rather interact with each other, exhibiting preferential orientations. Overall, DFT methods and 1D NMR data allowed us to clarify aspects related to equilibrium processes in solution that could not be predicted by a simple look at the X-ray structures of these complexes.

1. INTRODUCTION

Metallacrowns (MCs) are a class of self-assembled complexes that in recent years has gathered a lot of attention due to their interest in the areas of bioimaging, catalysis, single-molecule magnetism and lanthanide luminescence.[1-11] MCs are the inorganic analogues of crown ethers,

in which the $[C\text{-}C\text{-}O]_n$ repetition unit is replaced by $[M\text{-}N\text{-}O]_n$. As in their organic counterparts, the oxygen atoms pointing towards the center of the macrocyclic ring are highly preorganized for the complexation of metal cations, from alkali metals to transition ones, to lanthanides and actinides.[12–15]

Lanthanide(III) 12-MC-4 complexes assembled using salicylhydroxamate (Shi^{3-}) and Ga^{III} as the ring metal ($\{Ln^{III}(RO)_4[12\text{-}MC_{GaIII(N)Shi}\text{-}4]\}^-$) have very recently received attention for the development of new luminescent molecules.[1,9,16] In these complexes ancillary carboxylates (RO^-) bridge between the core ion and the ring metals, in this way fulfilling the coordination requirements of the lanthanide ions (often found 8-coordinated in these complexes).[9,17,18]

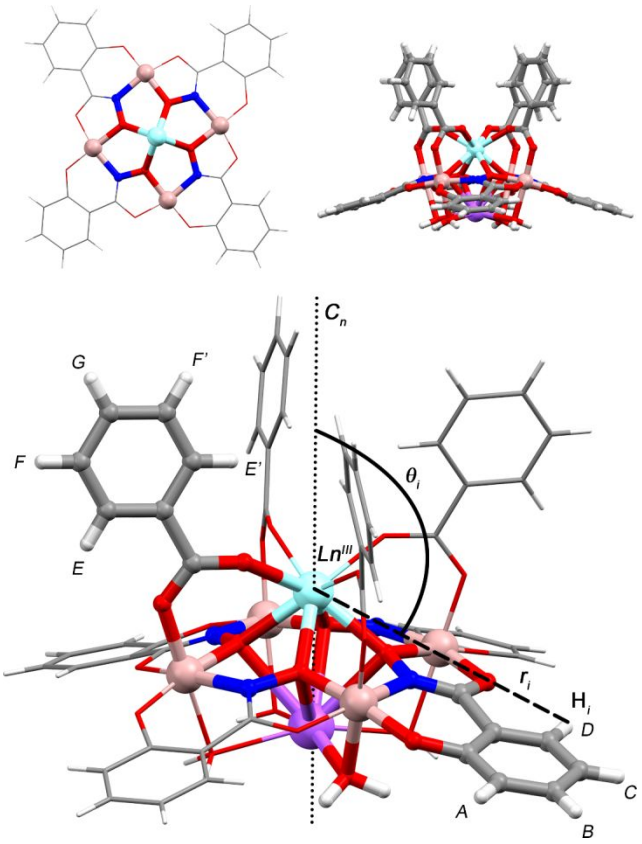

Figure 1. X-ray crystal structure of $Y^{III}Na^{I}(OBz)_4[12\text{-}MC_{GaIII(N)Shi}\text{-}4](H_2O)_4\cdot 6DMF$ complexes ($\mathbf{Y^{III}\text{-}1}$). Top (upper left) and side views (upper right) of the MC scaffold (benzoate residues were excluded in the top view, disordered Shi^{3-} residues and DMF molecules were omitted for clarity). Lower panel: schematic representation of the geometric parameters r_i and θ_i in $\mathbf{Y^{III}\text{-}1}$ or $\mathbf{Ln^{III}\text{-}1}$ complexes. The principal magnetic axis of the molecule was considered equivalent to the Ln^{III}-Na^{I} direction. Positions labelled with A-F correspond to observable protons in ^1H NMR spectra. Cyan: Y^{III}. Brown: Ga^{III}. Purple: Na^{I}.

Given their biotechnological potential, the study of the stability and the structure in solution of these complexes is pivotal. In this context, the presence of a lanthanide ions opens a window on the study of structural investigations in solution of these compounds using ^{1}H NMR. The analysis of the paramagnetic shift operated by the lanthanide cations, and in particular the pseudocontact (dipolar) contribution, carries truly precious structural information. The presence of a paramagnetic Ln^{III} center produces a shift in the observed resonance frequency of a nucleus in a coordinated ligand (δ_{Ln}^{obs}) that is the sum of a diamagnetic (δ_{Ln}^{dia}) and a paramagnetic contribution (δ_{Ln}^{para}) or Lanthanide Induced Shift (LIS). The δ_{Ln}^{para} term is in turn the sum of two contributions: the Fermi-contact contribution which depends on the electron density of the unpaired electron close to the observed NMR nucleus (δ_{Ln}^{FC}), and the pseudocontact contribution which originates from dipolar interactions between the spin of unpaired electrons and the spin angular momentum of the NMR nucleus (δ_{Ln}^{PC}). Following Bleaney's theory and its approximations, the pseudocontact contribution to the observed chemical is related to the structure of the lanthanide complex through **Equation 1**.[19–23]

$$\delta_{Ln}^{PC}(i) = C_J(Ln) \cdot B_{Ln} \cdot \frac{3cos^2\theta_i - 1}{r_i^3} \qquad (1)$$

where C_J(Ln) is the Bleaney's constant for the examined lanthanide ion and B_{Ln} is the crystal field parameter.[24] The $(3\cos^2\theta_i-1)/r_i^3$ is often referred to as geometric term or $G(i)$, where i identifies a proton under observation, r_i is the distance between the i proton and the paramagnetic center, and θ_i is the angle between the proton, the paramagnetic center and the principal magnetic axis of the complex (**Figure 1**). Since $\mathbf{Y^{III}}$**-1** is isostructural with $\mathbf{Ln^{III}}$**-1**, the δ_{Ln}^{para} contribution can be calculated using Y^{III} as the diamagnetic reference ($\delta_{Ln}^{dia} \approx \delta_{Y}^{obs}$):[25,26]

$$\delta_{Ln}^{para}(i) = LIS(i) = \delta_{Ln}^{PC}(i) + \delta_{Ln}^{con}(i) \cong \delta_{Ln}^{obs}(i) - \delta_{Y}^{obs}(i) \qquad (2)$$

For an isostructural series of lanthanide complexes such as 12-MC-4, which present a 4-fold axial symmetry, an efficient method of extracting the pseudocontact shift contributions of the Ln^{III} ions from the δ_{Ln}^{para} is the "all lanthanides" method.[27,28] The applicability of this method is general since it does not rely on the Bleaney's constants or their ratio, unlike Reilley's method or most other pseudo-contact/contact shift separation techniques.[29,30]

As recently reported in literature, NMR can be a powerful tool for the evaluation of structural features also for highly paramagnetic metallacrown compexes.[31] Also, we recently and successfully applied the "all lanthanides" method for the analysis of the NMR features of a series

of Mn^{III} paramagnetic complexes $Ln^{III}Na^{I}(OAc)_4[12\text{-}MC_{MnIII(N)Shi}\text{-}4](H_2O)_4\cdot 6DMF$, which allowed us to clarify several structural features of the complexes in solution.[28] While this was a significant achievement, the presence of highly paramagnetic Mn(III) complexes influenced the magnetic properties of the Ln(III). Thus, a diamagnetic ring metal analogue is necessary to develop the theory of this system fully.

Herein, we report the synthesis and structural characterization, both in solution and in the solid state, of trimetallic $Ln^{III}Na^{I}(OBz)_4[12\text{-}MC_{GaIII(N)Shi}\text{-}4]$ complexes containing four salicylhydroxamate ligands and four benzoate anions. The lanthanide ions were La^{III}-Lu^{III}, except Ce^{III} and Pm^{III}, and Y^{III}. In particular, we aimed to elucidate the NMR features of these MCs by a deep analysis of their spectra, and to correlate their solid-state structure with structural information obtained through ^{1}H NMR. We also correlated the data obtained from the NMR analysis with the solution structure obtained by computational DFT methods, with the aim of determining the degree of fluxionality and the structural rearrangements occurring in solution. By isolating different lanthanides in the same, nearly isostructural host, we are now able to extract parameters that will allow application, in general, of easily accessible 1D ^{1}H NMR data and DFT models in order to assess the structure in solution of lanthanide-containing systems.

2. EXPERIMENTAL SECTION

2.1 Materials and Methods. All reagents and solvents were commercial reagent grade chemicals and used without further purification. Gallium(III) nitrate was considered octa-hydrated ($Ga(NO_3)_3{\cdot}8H_2O$), based on studies reported elsewhere.[32] Lanthanide nitrate salts have been used as sources of Ln^{III} ions ($Ln(NO_3)_3{\cdot}xH_2O$, x = 6 for La^{III}-Gd^{III} and Y^{III}, and x = 5 for Tb^{III}-Lu^{III}). Elemental analysis of the isolated metallacrown batches were performed on Thermofisher Scientific Flash Smart CHNS (sample mass 2-3 mg). Electrospray ionization mass spectra (ESI-MS) of MC complexes (dissolved in methanol) were collected on a Micromass LCT TOF electrospray ionization mass spectrometer, using a capillary voltage of 3500 V and a desolvation temperature of 350 ˚C. Samples (40 μM) were injected through direct infusion using a syringe pump at 11 μL/min, and the spectra were recorded in full scan analysis mode in the range *m*/*z* 100–2000.

2.2 General preparation of $Ln^{III}Na^{I}(OBz)_4[12\text{-}MC_{Ga^{III}(N)Shi}\text{-}4](H_2O)_x(DMF)_y$ (Ln^{III}-1). Salicylhydroxamic acid (30.5 mg, 0.20 mmol) and sodium benzoate (82 mg, 0.57 mmol) were dissolved in 5 mL of a 1:1:0.25 DMF/MeOH/pyridine solution. $Ga(NO_3)_3{\cdot}8H_2O$ (80 mg, 0.20

mmol) was dissolved in methanol and added to the solution under stirring. After 5 minutes, $Ln(NO_3)_3 \cdot xH_2O$ (0.05 mmol) was dissolved in 1 mL of methanol and was added the mixture and stirred for about 5 minutes. NaCl (50 mg, 0.85 mmol) dissolved in the minimum quantity of water and 1 mL of methanol was finally added to the solution, which was concentrated at RT and crystalized at -4 ˚C. Slow evaporation of the solvents gave crystals suitable for X-ray diffraction analysis after a couple of days. The complexes were isolated with yields between 10-20%. In the complex formula, x resulted 3 for **Dy^{III}-1** and 4 for all the other **Ln^{III}-1**, while y resulted 5 for **Dy^{III}-1** and 6 for all the other **Ln^{III}-1**. Results of analyses on **Ln^{III}-1** complexes are reported as Supporting Information.

2.3 X-ray diffractometry. Single crystal X-ray diffraction data of the $Ln^{III}Na^{I}(OBz)_4$[12-$MC_{Ga^{III}(N)Shi}$-4]$(H_2O)_4 \cdot 6DMF$ series (**Ln^{III}-1**) where Ln^{III} stands for Ho^{III}, Er^{III}, Lu^{III} and Y^{III}, $Dy^{III}Na^{I}(OBz)_4$[12-$MC_{Ga^{III}(N)Shi}$-4]$(H_2O)_3 \cdot 5DMF \cdot 3MeOH$ (**Dy^{III}-1**), and of $Tb^{III}Na^{I}(Op\text{-}Tol)_4$[12-$MC_{Ga^{III}(N)Shi}$-4]$(H_2O)_4 \cdot 4DMF$ (**Tb^{III}-3**) were collected at 150 or 200 K on a Bruker D8 Photon II X-Ray diffractometer (Kα(Mo); λ = 0.71073 Å) equipped with a low temperature device. The intensity data were integrated from several series of exposure frames covering the sphere of reciprocal lattice.[33] Absorption correction was applied using the program SADABS.[34] The

structures were solved with ShelxT and refined on F^2 with full-matrix least squares (ShelxL), using the Olex2 software package.[35–37] The analysis of the structures (including distances and angles measurements) were carried out using the Mercury 2020.1 software package.[38] In Y^{III}-1, Ho^{III}-1, Er^{III}-1, and Lu^{III}-1 the salicylhydroxamate moiety was found disordered over two positions and refined with site occupancy factors of 0.5 each. Also, in those structures the presence of cavities was determined, and the solvent was modelled by using the Platon-squeeze program,[39] which gave voids corresponds approximately to 2 DMF molecules/cell for each structure. Y^{III}-1, Tb^{III}-3, Ho^{III}-1 and Lu^{III}-1 were refined with suitable twin matrixes. Non hydrogen atoms were refined with anisotropic thermal parameters. In all complex structures, hydrogen atoms were placed at their calculated positions. A summary of data collection and structure refinement of the complexes presented in this work is reported in **Table S3-5**.

2.4 NMR spectroscopy. ^{1}H NMR, (1D-, 2D-COSY and PGSE), and ^{23}Na NMR spectra were recorded in DMSO-d_6 on a Bruker Avance 400 spectrometer, using standard pulse sequences. Diffusion NMR spectra were obtained using a stimulated echo sequence with bipolar gradient. Chemical shifts (δ, ppm) were referenced to residual DMSO resonances, and the spectral window ranged from −50 ppm to +80 ppm. NMR spectra processing and analysis was performed

using the MestreNova 14.1 program.[40] All least-squares regression analyses (calculations through the "all lanthanides" method) were performed using OriginPro 8.[27,41]

2.5 DFT geometry optimizations. DFT geometry optimizations were performed using the GAUSSIAN software package.[42] Calculations were performed employing hybrid DFT with different exchange-correlation functionals (B3LYP, ωB97XD and M06-2X), with and without the application of Polarizable Continuum Model (PCM) for the evaluation of solvent effects.[43–46] The geometry optimizations were performed starting from the X-ray experimental geometry of $\mathbf{Y^{III}}$**-1** . The crystal structure of $\mathbf{Y^{III}}$**-1** exhibited two disordered images, and they were both considered for the optimization. Both model structures converged to the same optimized geometry. Furthermore, two model systems were used, namely one with the Na^{I} ion coordinated to the MC cavity oxygen atoms on the concave side of the domed MC scaffold (including coordinated water molecules), and one without the Na^{I} ion. The SDD basis set was used for Ga, def2-TZVP for Y (with MWB28 core potential for both) and the 6-31G basis set for all the other elements (C, H, N, O and Na).[47,48]

3. RESULTS AND DISCUSSION

3.1 Molecular Structures. The **Ln^{III}-1** complexes of Ho^{III}, Er^{III} and Lu^{III} were also analyzed through X-ray diffraction, and they resulted isostructural with **Y^{III}-1** in the solid state (**Figure 1**). The structures are C_4 symmetrical with the Shi^{3-} residues statically disordered over two positions with occupancies 0.5 each. The core Ln^{III} ion is side-on coordinated to the dome shaped MC scaffold at the convex side, with OBz^- ions bridging between the lanthanide and the ring Ga^{III} metal. One Na^I ion is coordinated on the concave side of the MC. An in-depth description of the structural features of the complexes is reported in the Supporting Information (**Figures S1-S13**).

In these molecules we have labelled the hydrogen atoms of the Shi^{3-} ligand with the letters A-D, and with E-G the benzoate hydrogen atoms (**Figure 1** and **Scheme 1**). The Dy^{III} complex, although not isostructural with the other **Ln^{III}-1** complexes, exhibits only subtle structural differences, *i.e.,* a more flattened MC scaffold and one DMF coordinated to a ring Ga^{III} ion in place of a water molecule.

We have also isolated the deuterated analogs of **Ln^{III}-1** complexes in which the Shi^{3-} ligand has deuterium in place of ^1H in position B (**Ln^{III}-2** series), and Ln^{III}[12-MC-4] with *p*-toluate as the bridging carboxylate ligand (**Ln^{III}-3** series), for which **Tb^{III}-3** presents a solid-state structure

analogous to that of the **Ln^{III}-1** complexes (the synthesis of **Ln^{III}-2** and **Ln^{III}-3** complexes is reported in the Supporting Information).

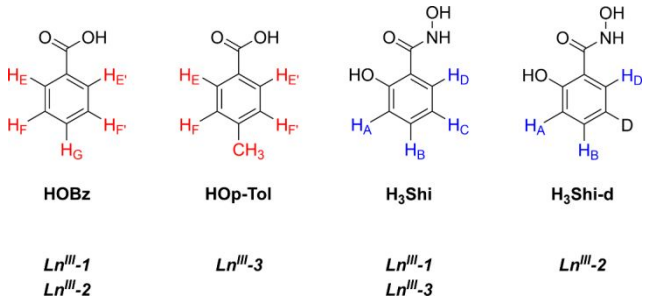

Scheme 1. Schematic representation of the ligands (left: BzO^-, right: Shi^{3-}) used in this work. Lettering scheme of protons is reported. The series of complexes for which the ligands are used are reported in italics.

The structures of the Y^{III}, Dy^{III}, Ho^{III}, Er^{III} and **Lu^{III}-1** complexes were determined by X-ray diffraction. Interestingly, **Lu^{III}-1** represents the first [12-MC_{GaIII}-4] complex to ever be characterized by X-ray diffraction to date, with the other Lu^{III}-MCs containing Al^{III} (12-MC-4) or Cu^{II} (15-MC-5) as ring metals.[49,50] The complex is isostructural with the other complexes of the **Ln^{III}-1** series. However, the smaller ionic radius of lutetium(III) makes the Ln^{III}-O_{Bz} and Ln^{III}-O_{Shi} distances (2.25 and 2.32 Å, respectively) shorter than the same in the other complexes

of the series which are in the 2.28-3.31 Å and 2.34-2.37 Å range, respectively. Also, Lu^{III} is better encapsulated in the cavity compared to the other ions as shown by the smaller displacement from the cavity center. Lu^{III} is in fact 1.45 Å distant from the mean plane of the cavity Shi^{3-} oxygen atoms ($O_{Shi}MP$) compared to 1.46-1.52 Å of the other **Ln^{III}-1** structures (**Table S2**). Importantly for interpreting NMR analyses (see below), it is worth noting that the Shi^{3-} residues are disordered in two positions in all the Ho^{III}-Lu^{III} and Y^{III} structures. In-depth structural description of all the complexes is presented in the Supporting Information.

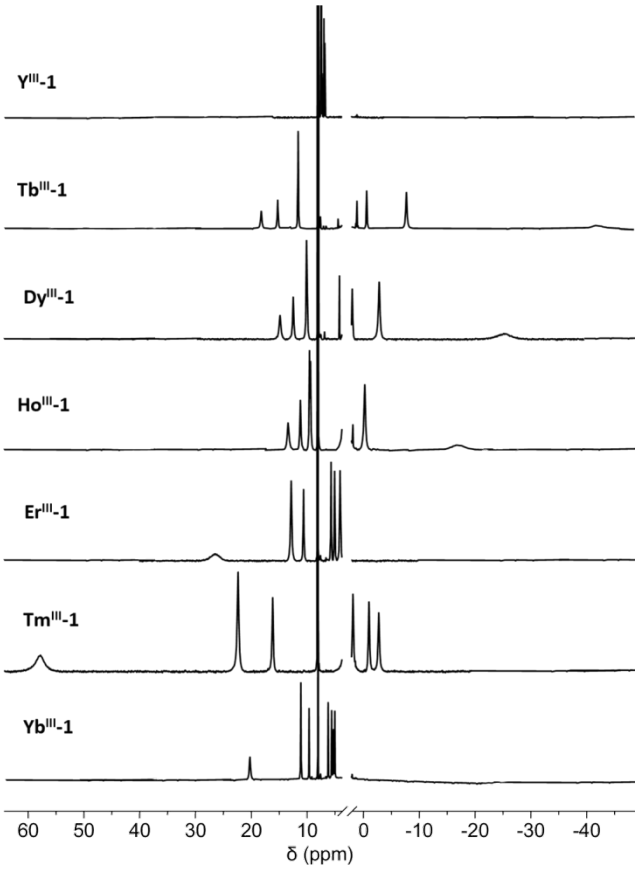

Figure 2. From top to bottom: ^{1}H NMR spectra of **Y^{III}-1**, **Tb^{III}-1**, **Dy^{III}-1**, **Ho^{III}-1**, **Er^{III}-1**, **Tm^{III}-1** and **Yb^{III}-1**. The region 2.00 - 3.50 ppm excluded (solvent signals only).

3.2 NMR Characterization. The proton 1D- and 2D-COSY NMR spectra DMSO-d_6 of thirteen $Ln^{III}Na^{I}(OBz)_4[12\text{-}MC_{GaIII(N)Shi}\text{-}4](H_2O)_4\cdot 6DMF$ complexes (**Ln^{III}-1**) were examined, where Ln^{III} is La^{III}-Lu^{III} (except Ce^{III} and Pm^{III}), and Y^{III}.

The 1D spectra for **Ln^{III}-1** of heavier lanthanides (Ln^{III} = Tb^{III}-Yb^{III}) are reported in **Figure 2** along with that of **Y^{III}-1**. All the recorded ^{1}H NMR spectra of the **Ln^{III}-1** complexes present a set of seven chemically non-equivalent proton signals as previously observed for the [12-$MC_{MnIII(N)Shi}$-4] analogs, consistent with the presence of an average C_4 symmetry axis in in solution. The E/E' and F/F' protons (**Figure 1**) are chemically equivalent, suggesting fast exchange between these positions, although we will show below that other chemical exchange phenomena occur in these molecules. The ^{1}H NMR spectra of the entire series of **Ln^{III}-1** complexes are shown in the Supporting Information (**Figure S26-S61**).

Due to the paramagnetism of the Ln^{III} ions, the signals are spread over a large spectral window that in the case of heavier lanthanides ranges from -40 to +60 ppm. Conversely, the signals of **Y^{III}-1**, **La^{III}-1**, and **Lu^{III}-1** are in the spectral range expected for diamagnetic species and their spectra will be discussed more in detail below (6.50 - 8.00 ppm, **Figure S15**). The ^{1}H NMR spectra of **Ln^{III}-1** with paramagnetic lanthanides show band widths of ca. 40 Hz (except for **Gd^{III}-1**).[†] Therefore, the spectra of these complexes resulted in better resolved resonances than those observed previously for the analogs containing Mn^{III}, namely $Ln^{III}Na^{I}(OAc)_4$[12-$MC_{MnIII(N)Shi}$-4] complexes. Those complexes actually exhibited signals of ca. 500 Hz band width as the result of

the relaxation effects operated by the $[Mn^{III}]_4$ system. Also, in the spectra of **Ln^{III}-1** with Pr^{III}, Nd^{III}, Sm^{III} and Eu^{III} the signals are well-resolved, and the H-H coupling constants were observed.[25]

With the purpose of signal assignment (see below) we also registered the spectra of **Ln^{III}-2** complexes (Shi^{3-} ligand deuterated in C position), with Ln^{III} being Eu^{III}-Yb^{III} and Y^{III} (**Figure 3** for **Y^{III}-2**). The ^{1}H NMR spectra of the complexes are reported as Supporting Information (**Figure S41-S51**). The ^{1}H NMR spectra are identical to those of **Ln^{III}-1** except for the fact that, due to the presence of 85% deuteration on the hydrogen in position C, one resonance has as an integral ca. 15% for **Ln^{III}-2** compared to that of **Ln^{III}-1** (**Figure 3**). Finally, we collected the spectra of **Ln^{III}-3** complexes, with Ln^{III} being Tb^{III}, Dy^{III} and Y^{III} (see Supporting Information, **Figure S48-50**). The ^{1}H NMR spectra of **Y^{III}-3** is also reported in **Figure 3**: the presence of a signal at 2.28 ppm (CH_3) and the signals pattern provided further information used for signal assignment (see below).

Homonuclear 2D COSY NMR spectra could be examined for **Ln^{III}-1**, **Ln^{III}-2** and **Ln^{III}-3** complexes with lighter lanthanides only, or Y^{III} (see Supporting Information, **Figures S51-S61**). Conversely, we did not observe 2D COSY cross peaks for heavier lanthanides (Tb^{III}-Tm^{III}) as a

consequence of the enhanced ^{1}H relaxation conferred by these lanthanide ions.[25] We also acquired PGSE data on **Y^{III}-1** which allowed to rule out dissociation phenomena involving BzO^- ions in DMSO (**Figure S70**). Actually, the normalized intensity of all aromatic signals versus the square of the gradient strength follows the same exponential decay, showing that benzoate and Shi^{3-} ligands are assembled in the same molecular entity in solution, and no appreciable dissociation of benzoate ions is observed (**Figure S71**).

Finally, ^{23}Na NMR spectral data were collected for **Ln^{III}-1** (Supporting Information, **Figure S61-S68**). These spectra show that the line widths are in the range from 75-90 Hz for **Ln^{III}-1**, irrespective of the presence or absence of a paramagnetic lanthanide with similar chemical shift values, which are intermediate between 180-500 Hz for the Na^I adducts with 18-C-6 and 15-C-5 in methanol, and 59 Hz for NaCl in DMSO.[51–54] We, therefore, believe that for our **Ln^{III}-1** complexes in DMSO the Na^I ion is primarily dissociated in solution, as previously observed for $Ln^{III}Na^{I}$[12-$MC_{MnIII(N)Shi}$-4]$(H_2O)_4$·6DMF complexes.[28]

3.3 Assignment of resonances. The first step in the analysis of 1D NMR spectra was to assign all resonances of the diamagnetic complexes to protons A-G (**Figure 1**). Based on the ^{1}H COSY NMR spectrum of **Y^{III}-1** complex, the Shi^{3-} set of signals resulted 6.87, 6.72, 7.24 and 7.87 ppm

(**Figure 3** and **Table S8**, Supporting Information), while those of BzO^- resulted 7.34, 7.45 and 7.92 ppm. An unambiguous assignment of the C proton resonance of Shi^{3-} was possible observing the low intensity of the resonance at 6.72 ppm of $\mathbf{Y^{III}}$**-2** (85% deuterated, **Figure 3**). The complete assignments of both Shi^{3-} and benzoate protons (**Figure 3** and **Table S8**) were obtained based on the signal multiplicity and 2D COSY correlations. An ultimate confirmation of the benzoate protons arose examining the resonances of compound $\mathbf{Y^{III}}$**-3** where p-$TolO^-$ anions are present in place of BzO^- (*i.e.,* the signal of the G proton at 7.45 ppm was absent in the spectrum of $\mathbf{Y^{III}}$**-3** while that of the CH_3 group at 2.28 ppm was observed).

$\mathbf{Lu^{III}}$**-1** and $\mathbf{Y^{III}}$**-1** have almost identical ^1H NMR spectra, thus confirming the goodness in the use of the latter as a diamagnetic reference (**Table S9** and **Figure S15**, Supporting Information). On the contrary, the ^1H NMR spectrum of $\mathbf{La^{III}}$**-1** (also diamagnetic) presents significant differences in the position of the signals with respect of that of $\mathbf{Y^{III}}$**-1** (**Figure S15**). Although we may interpret these differences with the tendency of La^{III} to adopt a 9-coordination instead of an 8-coordination, all attempts to crystallize $\mathbf{La^{III}}$**-1** were unsuccessful and therefore further comments are not possible.

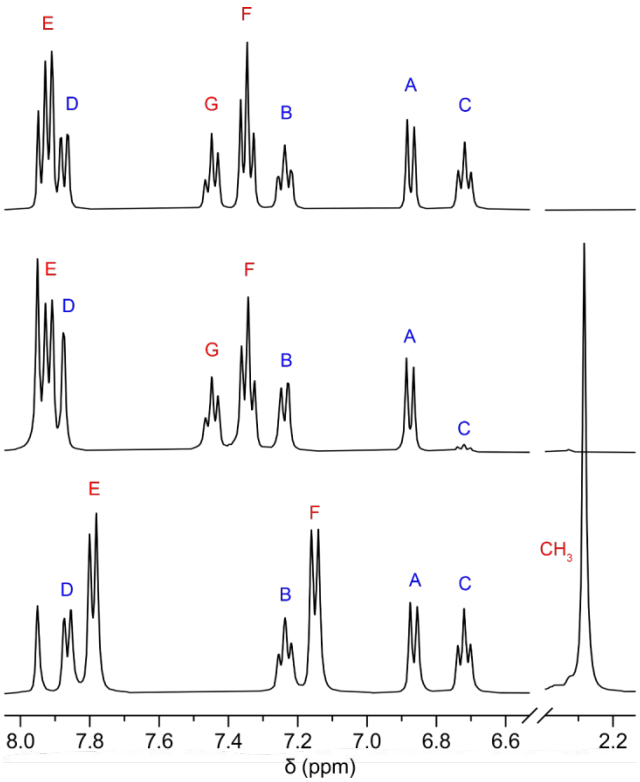

Figure 3. Stacked ^{1}H NMR spectra of $\mathbf{Y^{III}}$**-1**, $\mathbf{Y^{III}}$**-2** and $\mathbf{Y^{III}}$**-3**. Signals are labelled from A to G and the signals of the Shi^{3-} ligands are highlighted in blue, whereas the signals of the BzO^{-} ligands are highlighted in red, see **Scheme 1**.

The marked differences between the 1D ^{1}H NMR spectra of $\mathbf{Ln^{III}}$**-1** of heavier lanthanides (**Figure 2**) show that the paramagnetic contribution (δ_{Ln}^{para}) is dominant in the observed NMR signals (δ_{Ln}^{obs}), and in some complexes such as $\mathbf{Tb^{III}}$**-1** or $\mathbf{Tm^{III}}$**-1** may be up to 50 ppm. This prevented a naked-eye assignment of the resonances for these lanthanides. Here below we

describe the strategy for the assignment of the signals for **Ln^{III}-1** of heavier lanthanides, while that for lighter lanthanides is described in the Supporting Information (Pr^{III}-Eu^{III}, **Figure S18**).

As a first approximation, for each *i* proton in **Ln^{III}-1** the $\delta_{Ln}^{para}(i)$ contribution roughly equals $\delta_{Ln}^{PC}(i)$, which considers $\delta_{Ln}^{PC}(i) \gg \delta_{Ln}^{con}(i)$. This, at least for heavier lanthanides, is sufficiently good given their large Bleaney's constants (**Equations 1** and **2**). Also, the sign of $\delta_{Ln}^{PC}(i)$ for an *i* proton depends on both the sign of C_J and that of G(*i*) as shown by **Equation 1**, and therefore the Shi^{3-} and BzO^{-} signal in each spectrum could be discriminated. Actually, the sign of C_J is known (negative for the oblate Tb, Dy and Ho, positive for the prolate Er, Tm and Yb). The evaluation of the crystal structures showed that for the Shi^{3-} protons θ_i are greater than 54.7° and therefore for a prolate ion such as Yb^{III} (*i.e.,* $C_J > 0$) the proton resonances are expected to be upfield shifted with respect to the signals of **Y^{III}-1**, which indeed was observed. On the contrary, BzO^{-} protons θ_i are lower than or close to 54.7° and therefore the three resonances E-G for prolate ions are downfield shifted (both the $G(i)$ term and the Bleaney's constant C_J are positive, **Figure S16**). The opposite is observed for oblate ions. As a partial result we found that the resonances of the four Shi^{3-} protons are in the spectral windows -3 to +6 ppm for Tb^{III}-Ho^{III} (positive C_J), whereas for Er^{III}-Yb^{III}, which possess a negative C_J, the resonances are observed

between +9 and +18 ppm. Conversely, the BzO^- resonances are in the +9 to +57 ppm window for Tb^{III}-Ho^{III}, or in the -42 to +3 ppm window for Er^{III}-Yb^{III} (see **Figure S17**, Supporting Information).

The final assignment was performed by the evaluation of $\langle G(i)\rangle$ [‡] values, that are the average value of G(*i*) over the four corresponding protons in the same *i* position (eight positions for E and F protons) calculated from X-ray crystal data of **Ln^{III}-1**:

$$\langle G(i)\rangle = \sum\left(3cos^2\theta_i - 1\right)/r_i^3 \qquad (3)$$

Since the four Shi^{3-} protons reside at approximately equal θ_i values, it results that the closer a proton is to the lanthanide ion (*i.e.,* the smaller r_i^3) the larger is its associated $\langle G(i)\rangle$ and, therefore, its pseudocontact shift. Based on this information, the largest pseudocontact shift is experienced by the D proton (**Table S18**), followed by protons A and C. Proton B is the most distant from the Ln^{III} ion, thus experiencing the smallest pseudocontact contribution. These assignments are summarized in **Tables S12** and **S18** and were confirmed by examination of NMR data of the deuterated **Ln^{III}-2** complexes where the signal of C proton is missing. As for the signals of the BzO^- ligands, the peak that experiences the biggest shift (*i.e.,* resonance 1, **Figure**

S16) was assigned to proton E for all compounds, which is the closest to the Ln^{III} ion, thus associated with the largest calculated $\langle G(i) \rangle$ (See Table 13). The resonances of protons F and G were easily assigned by inspection of the peak integrals (two and one protons, respectively).

3.4 Calculation of pseudocontact shift. The calculation of the Fermi contact and pseudocontact contributions to the chemical shifts for Ln^{III}-1 complexes was performed using the "all lanthanides" method.[27,28] Data treatment presented here is limited to heavier lanthanides for which the pseudocontact contribution dominates over the Fermi one. The treatment for lighter lanthanides is reported in the Supporting Information. Following the "all lanthanides" method, we first plotted the $\delta_{Ln}^{para}(i)$ reported in Table S13 as a function of the reference $\delta_{Yb}^{para}(i)$ (Plot I, Figure 4).[27] Linear regressions forced through the origin were performed on data related to each lanthanide and the calculated slopes m_{Ln} are reported in Table S13. The physical meaning of m_{Ln} (within the limits of validity of Bleaney's theory) is $m_{Ln} = C_J(Ln)/C_J(Yb)$.[55] However, more realistically m_{Ln} would reduce to $B_{Ln}C_J(Ln)/B_{Yb}C_J(Yb)$ since B_{Ln} is not expected to be strictly constant throughout the series, as observed for the isostructural $Ln^{III}Na^{I}(OAc)_4$[12-$MC_{Mn^{III}(N)Shi}$-4]$(H_2O)_4$·6DMF compounds, and C_J values of lanthanides in the complexes may differ from those of the free ion.[28]

Following the "all lanthanides" method, we then plotted the $\delta_{Ln}^{para}(i)/\langle S_z\rangle_{Ln}$ values as a function of $m_{Ln}/\langle S_z\rangle_{Ln}$ (Plot II, **Figure 5**) in which each line relates to one specific A to G proton. The points were fitted through linear regression without constraining the lines passing through the origin. The calculated slope and intercept values, respectively, are labeled M_i and Q_i and are reported in **Table S15** and S11. Pseudocontact and Fermi contact contributions to the chemical shift of the proton signals were then calculated:[28]

$$\delta_{Ln}^{PC}(i) = m_{Ln} \cdot M_i \quad (4)$$

$$\delta_{Ln}^{con}(i) = \delta_{Ln}^{obs}(i) - \delta_{Ln}^{PC}(i) \quad (5)$$

The values of $\delta_{Ln}^{con}(i)$ and $\delta_{Ln}^{PC}(i)$ calculated by means of **Equations 4** and **5**, respectively are also reported in **Table S15** and **S16**. Overall, as expected, we found values which confirm that the δ_{Ln}^{PC} contribution dominate over δ_{Ln}^{con}. Expectedly, oblate lanthanides (Tb^{III}, Dy^{III}, Ho^{III}) present δ_{Ln}^{PC} which are opposite in sign than those of prolate ones (Er^{III}, Tm^{III}, Yb^{III}).

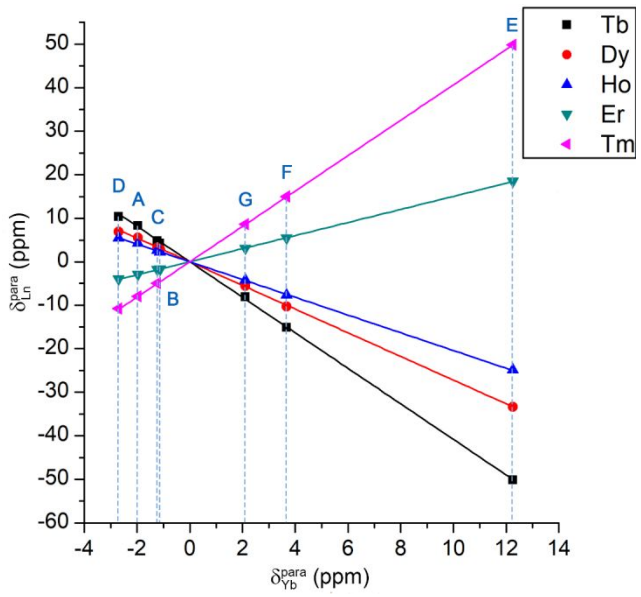

Figure 4. Plot of $\delta_{Ln}^{para}(i)$ as a function of $\delta_{Yb}^{para}(i)$ ("Plot I") for $Ln^{III}Na^{I}(OBz)_4$[12-$MC_{GaIII(N)Shi}$-4]$(H_2O)_4$·6DMF (where Ln^{III} = Tb^{III}-Tm^{III}). The A-G labels reported in blue refer to the ligand protons in the corresponding positions.

The M_i values determined through the "all lanthanides" method relate with the geometric term $G(i)$ values through the relationship $M_i/M_j = G(i)/G(j)$. Consequently, for each **Ln^{III}-1** complex the M_i/M_j ratio obtained by NMR contains the structural information associated to the $G(i)$ parameters. Normalized M_i values (= M_i/M_B since M_B is the smallest for all complexes) determined by NMR are reported in **Table 1** along with the corresponding normalized $G(i)$

values obtained from the crystal structures of **Ln^{III}-1** complex. M_i values should correspond to the $G(i)$ values for a scale factor γ (*i.e.*, $M_i = \gamma \cdot G(i)$) where in theory $\gamma = B_{Ln} \cdot C_i(\mathrm{Yb})$. Here below we will show how we used γ as an empirical least square parameter to compare structural models of the complexes with NMR data. Finally, since the M_i and the $\langle G(i) \rangle$ values have the same sign, the consistency between the NMR observations, the X-ray structural data and the signal assignment are in full agreement.

Table 1. Normalized M_i values of the protons obtained from NMR data and normalized geometric $\langle G(i) \rangle$ parameters calculated for the X-ray structure of **Y^{III}-1**, the **Y-rot** model and the ones of the three DFT models ($\langle G(i) \rangle$) that give the best agreement with the M_i values. The σ values are also reported (see equation 6).

Parameter	$i = H_A$	H_B	H_C	H_D	$H_{E/E'}$	$H_{F/F'}$	H_G	σ[a]
M_i	1.79	1.00	1.11	2.40	-11.12	-3.35	-1.91	-
$\langle G(i) \rangle$								
Y^{III}-1	1.56	1.00	1.11	2.05	-7.52	-2.28	-1.21	1.37
Y-rot	1.56	1.00	1.11	2.05	-2.31	-1.52	-1.21	11.7

Y-NaBP	1.62	1.00	1.16	2.40	-10.49	-3.29	-1.89	0.100
Y-BP	1.73	1.00	1.19	2.62	-12.41	-3.83	-1.94	0.142
Y-XP	1.72	1.00	1.19	2.65	-12.20	-3.91	-2.19	0.187

[a] See equation 6.

Noteworthy, the normalized X-ray $\langle G(i)\rangle$ values of Shi^{3-} protons reported in **Table 1** are much closer to the corresponding normalized M_i values than those of the benzoate protons (2-23 % difference for A-D protons, 24-39% for E-G). Having ruled out the dissociation of benzoates on the basis of PGSE data, we made the hypothesis that the larger difference between the M_i and $\langle G(i)\rangle$ values for benzoate protons arises from the free rotation of the phenyl ring of the BzO^- residues around the C-C axis. This free rotation agrees with the equivalence of two F and E protons in the NMR spectra but is not considered when the X-ray coordinates are used in calculating $\langle G(i)\rangle$. We, therefore, generated models based on the X-ray structure of $\mathbf{Y^{III}}$**-1** where the phenyl rings are rotated around the C-C axis of 45, 90 and 135 degrees compared to the main benzoate plane (**Figure S20**). The corresponding $\langle G(i)\rangle$ parameters were then calculated from **Equation 3** but as an average of the four models and are reported in **Table 1** as **Y-rot**. To most of our surprise, for **Y-rot** the normalized $G(i)$ values for E and F benzoate protons differ by 80%

and 55% from the experimental M_i compared to 33% and 32% for the **Y^{III}-1** crystal structure, respectively. Strikingly, the model with free rotation of the phenyl group, is a worse model in explaining NMR data compared to the **Y^{III}-1** crystal structure. This unexpected result suggests that the benzoate aromatic groups are not freely rotating in solution, but rather are spatially arranged in preferential positions or conformations. We therefore decided to investigate the solution structure of those complexes using DFT calculations, in search of other structural models to compare the NMR data with.

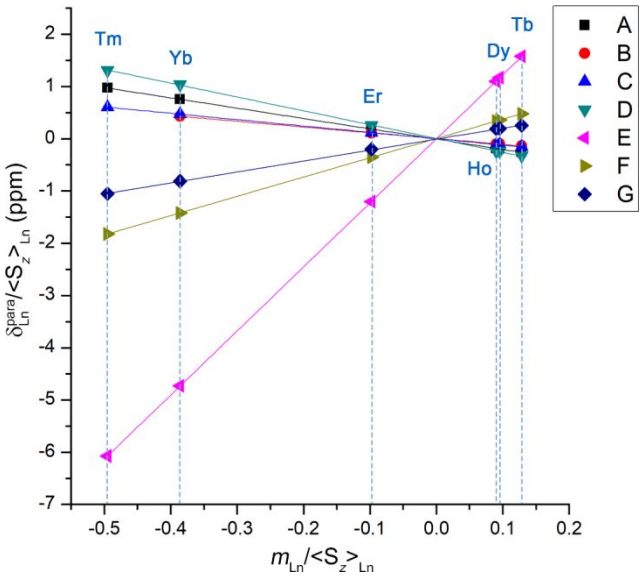

Figure 5. Plot of $m_{Ln}/\langle S_z \rangle_{Ln}$ vs $\delta_{Ln}^{para}(i)/\langle S_z \rangle_{Ln}$ ("Plot II") for $Ln^{III}Na^{I}(OBz)_4$[12-$MC_{GaIII(N)Shi}$-4]$(H_2O)_4$·6DMF (where Ln^{III} = Tb^{III}-Yb^{III}). Letters correspond to proton positions, while δ_{Ln}^{para} values for each lanthanide are on vertical dashed lines.

3.5 DFT calculations. DFT geometry optimization calculations were performed on the diamagnetic **Y^{III}-1** complex using the X-ray structure as a starting model. Three different density functionals were employed, namely B3LYP, ωB97XD and M06-2X, and the related models were labelled with B, X and M, respectively (see labels in **Table S17**). Beside the widely used B3LYP, the ωB97XD density functional contains dispersion correction, and it is suitable to model both short-range and long-range interactions. Similarly, the M06-2X density functional has proven to be employed for the description of non-covalent interactions and isomerization energies.[43,44,56] Finally, all models were optimized by considering either the presence or the absence of the Na^{I} ion, together with the four bridging water molecules. Representations of the DFT optimized geometries and description of the labelling scheme used are reported as Supporting Information (see also **Table S17**). A representative overlay of the X-ray structure of **Y^{III}-1** with the optimized model **Y-NaBP** is reported in **Figure S24**. Overlays between the solid state and DFT models are also reported in the Supporting Information. For all the calculated structures we calculated the normalized $\langle G(i) \rangle$, which are reported in **Table 1** and **Table S18**.

To evaluate which model best explains NMR data, we used the least square function σ (**Equation 6**) for each X-ray or DFT structure. The scale factor γ was considered a least square parameter: the smaller the σ value, the more the structural model is consistent with the NMR data.

$$\sigma = \sum_i [M_i - \gamma \cdot \langle G(i) \rangle]^2 \qquad (6)$$

The σ parameters are reported in **Table 1** along with the normalized M_i and $\langle G(i) \rangle$ of the three best models, namely **Y-XP, Y-BP** and **Y-NaBP**, which have a very similar σ value. The $\langle G(i) \rangle$ values for all X-ray structures and DFT models, including calculated γ parameters, are reported in **Table S18**. Interestingly, the three DFT models are characterized by a better agreement with the NMR data (lower σ values) than the experimental X-ray structures, **Table 1**. This can be tentatively explained by inspecting the crystal packing of $\mathbf{Y^{III}}$**-1**, which is characterized by the presence of a partial pi-stacking between the phenyl moieties of the MC and the DMF molecules (**Figure S14**). The pi-staking forces the MC platform to adopt a more planar arrangement with respect to the DFT optimized geometry. Indeed, the DFT geometry present a marked doomed shape of the MC scaffold.

Interestingly, the **Y-NaBP** model that bears the coordinated Na^{I} gives the best M_i vs. $\langle G(i) \rangle$ fit through **Equation 6**. However, the difference between the conformation and the least square σ values of **Y-BP** and **Y-NaBP** are very small (**Table 1**), which suggests that the coordination of sodium may not have a major role in determining the geometry of the MC. **Y-BP** and **Y-NaBP** (**Figure 6 a**) are close to C_4 symmetrical and the overall structure not significantly different to the crystal structure of $\mathbf{Y^{III}}$**-1**. Conversely, **Y-XP** (**Figure 6b**) presents a pseudo-C_2 symmetry with two alternated Shi^{3-} ligands deviating markedly from the four-oxygen cavity mean plane, while the remaining two are more coplanar.

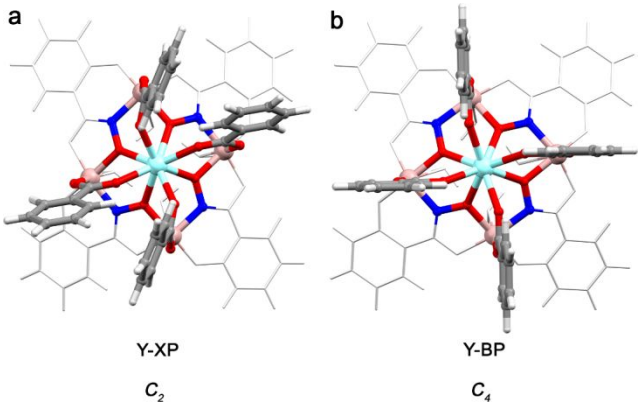

Figure 6. Representation of the conformation of the ligands in the **Y-BP** model (a) and in the **Y-XP** model (b). The structure of **Y-NaBP** is not reported as this model is extremely similar to the **Y-BP** one. The pseudo-symmetry of the models is reported in italics at the bottom. The interactions

between the benzoate residues are clearly visible in the pseudo-C_2 model and are however highlighted in the Supporting Information.

In the **Y-XP** model represented in **Figure 6** two out of the four benzoate ligands are approximately in the same position observed in the X-ray structure, while the remaining two (in alternate positions) show rotated phenyl residues which assume a bent conformation with respect to the MC mean plane. These conformational changes of the benzoate ions are accompanied by a conformational change of the MC scaffold, in which two alternate Shi^{3-} ligands are more coplanar and the remaining two more bent. These conformations are stabilized by CH···π interactions between adjacent BzO^- residues in agreement with the hypothesis that the benzoate ligands have preferential positions rather than being freely rotating in solution. Lastly, we determined that the **Y-XP** models is the most stable between the two best models as the single point energy of the model is lower than that of **Y-BP** both using the B3LYP and ωB97XD density functional (**Table S19**), thus proving that the **Y-BP** model is related only to a local

minimum on the Potential Energy Surface. Based on these observations we put forward the hypothesis that the geometry of the **Y-XP** conformation is likely the most abundant in solution but, due to the presence of an average four-fold symmetry in the NMR experiments, can go through a dynamic equilibrium. The prevalence of the **Y-XP** conformation is in full agreement with the observation that NMR data suggest that there is no free rotation of the phenyl groups of the carboxylates. The pseudo four-fold symmetrical **Y-BP** conformation is however possible intermediate in the dynamic equilibrium which involves the two **Y-XP** conformers (figure 7), being the calculated energy difference between the two models only 5.1 kJ mol^{-1} (ωB97XD density functional).

Further considerations on the nature of these conformers are not possible using the available data. However, it must be highlighted that the presence of multiple stable spatial orientations of the bridging benzoates can be of extreme importance to provide stability to dimeric or trimeric metallacrowns with carboxylate linkers bridging anions.[57,58] Also, the differences in the symmetry of the coordination environment could lead to interesting effects in the luminescent behavior of this class of compounds.[59]

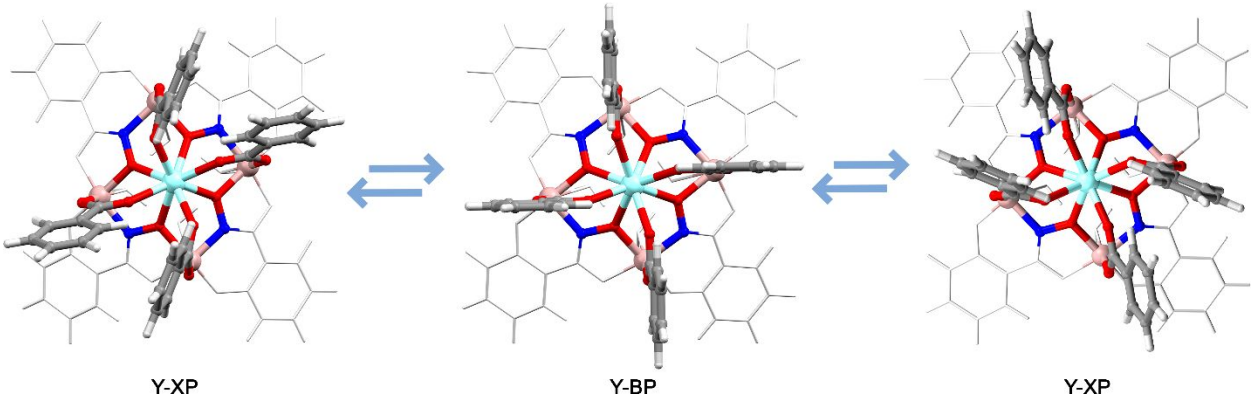

Figure 7. Representation of the fluxionality equilibrium between conformers. On the right the structures **Y-XP** which is pseudo-C_2 symmetrical, at the center the structure **Y-BP** which is pseudo-C_4 symmetrical. The conformer on the right is identical to the one on the left, rotated by 90°.

Overall, NMR data analyzed on the basis of crystal structures and DFT models suggest that fluxionality is likely present in these structures, but with a different involvement of the MC framework and the ancillary benzoate ions. While the former maintains roughly the same geometry, the benzoate ligands are freer to change their orientation and spatial arrangement. This in turn suggests that the Ln^{III}[12-$MC_{Ga^{III}(N)Shi}$-4] framework can sustain conformational adaptations that are larger from those predicted by the analysis of the X-ray structures. For these reasons these complexes are expected to be very interesting building blocks for the assembly of complex structures in which the spatial adaptation of the carboxylate ligands is required.

Conclusion

This paper presents an application of both the "all lanthanides" NMR data treatment and DFT analysis to a series of self-assembled metallacrowns of known structure. The analysis we have performed put together the three groups of information (NMR, DFT, X-ray structure) to elucidate the nature of structural adaptations that occur in solution. The average four-fold symmetry in solution consistent with the pattern in the ^{1}H NMR resonances is likely not strictly C_4 symmetrical as observed in the solid state. This average four-fold symmetry, consistent with the pattern in the ^{1}H NMR resonances, is rather the result of processes of fluxionality of the MC scaffold that presents two different orientations of the salicylhydroxamate ligands (also supported by the disorder in the X-ray structures). The NMR structural information could be rationalized using DFT optimized structures that suggested the presence of intramolecular C-H···π interaction of adjacent benzoate residues in C_2 symmetrical MC conformers.

The approach described in this work can be applied in the future to other classes of supramolecules that possess lanthanide ions in their structure. DFT structural models were used

to rationalize NMR information that were obtained by a fine treatment of simple 1D data. Also, the "all lanthanides" method allowed for this purpose to process the entire 1D NMR dataset as a whole, and to extract parameters that are correlated with the structure of lanthanide complexes without incurring in the limitations imposed by other methods of analysis.

ASSOCIATED CONTENT

Supporting Information. Experimental procedures for the synthesis of ligands and complexes; experimental details of X-ray structural studies; structural description of the complexes; X-ray crystallographic data; NMR characterization of the complexes (proton 1D and COSY spectra, proton PGSE experiments, ^{23}Na spectra); assignment of the signals for lighter lanthanides; "all lanthanides" method for lighter lanthanides; results of DFT calculations and representation of the structural models (PDF).

CCDC 2179628 and 2179795-2179799 contains the supplementary crystallographic data for this paper. These data can be obtained free of charge via www.ccdc.cam.ac.uk/data_request/cif, or by emailing data_request@ccdc.cam.ac.uk, or by contacting The Cambridge Crystallographic Data Centre, 12 Union Road, Cambridge CB2 1EZ, UK; fax: +44 1223 336033.

AUTHOR INFORMATION

Corresponding Author

* Matteo Tegoni – Department of Chemistry, Life Sciences and Environmental Sustainability, University of Parma, Parco Area delle Scienze 17A, 43124 Parma, Italy; orcid.org/0000-0002-9621-0410; Email: matteo.tegoni@unipr.it

* Vincent L. Pecoraro – Department of Chemistry, Willard H. Dow Laboratories, University of Michigan, Ann Arbor, Michigan 48109, United States; orcid.org/0000-0002-1540-5735; E-mail: vlpec@unipr.it

Author Contributions

All authors have given approval to the final version of the manuscript. ‡These authors contributed equally to this work.

Funding Sources

This work was supported by the National Science Foundation under grant CHE-2102046 to V.L.P. The research leading to these results has received funding from the European Community's Seventh Framework Programme (FP7/2013-2017) under grant agreement no.

611488. M.T. and V.L.P. thank the MAECI (Italian Ministry of Foreign Affairs and International Cooperation, Direzione Generale per la Promozione del Sistema Paese) for financial support through the bilateral Italy-USA project "Development of porous magnetic Metallacrowns for sensing applications".

Notes

The authors declare no conflicts of interest.

ACKNOWLEDGMENT

This work has benefited from the equipment and framework of the COMP-HUB and COMP-R Initiatives, funded by the 'Departments of Excellence' program of the Italian Ministry for University and Research (MIUR, 2018-2022 and MUR, 2023-2027).

REFERENCES

(1) Lutter, J. C.; Eliseeva, S. V.; Kampf, J. W.; Petoud, S.; Pecoraro, V. L. A Unique Ln(III){[3.3.1]Ga(III)Metallacryptate} Series That Possesses Properties of Slow Magnetic Relaxation and Visible/Near-Infrared Luminescence. *Chem. – A Eur. J.* **2018**, *24* (42), 10773–10783. https://doi.org/10.1002/chem.201801355.

(2) Lutter, J. C.; Lopez Bermudez, B. A.; Nguyen, T. N.; Kampf, J. W.; Pecoraro, V. L. Functionalization of Luminescent Lanthanide-Gallium Metallacrowns Using Copper-Catalyzed Alkyne-Azide Cycloaddition and Thiol-Maleimide Michael Addition. *J. Inorg. Biochem.* **2019**, *192* (October 2018), 119–125. https://doi.org/10.1016/j.jinorgbio.2018.12.011.

(3) D'Aléo, A.; Pointillart, F.; Ouahab, L.; Andraud, C.; Maury, O. Charge Transfer Excited States Sensitization of Lanthanide Emitting from the Visible to the Near-Infra-Red. *Coord. Chem. Rev.* **2012**, *256* (15–16), 1604–1620. https://doi.org/10.1016/j.ccr.2012.03.023.

(4) Trivedi, E. R.; Eliseeva, S. V.; Jankolovits, J.; Olmstead, M. M.; Petoud, S.; Pecoraro, V. L. Highly Emitting Near-Infrared Lanthanide "Encapsulated Sandwich" Metallacrown Complexes with Excitation Shifted toward Lower Energy. *J. Am. Chem. Soc.* **2014**, *136* (4), 1526–1534. https://doi.org/10.1021/ja4113337.

(5) Petoud, S. Novel Antennae for Luminescent Lanthanide Cations Emitting in the Visible and in the Near-Infrared: From Small Molecules to Polymetallic Lanthanide Containing Nanocrystals. *Chimia (Aarau).* **2009**, *63* (11), 745–752. https://doi.org/10.2533/chimia.2009.745.

(6) Eliseeva, S. V.; Bünzli, J. C. G. Lanthanide Luminescence for Functional Materials and Bio-Sciences. *Chem. Soc. Rev.* **2010**, *39* (1), 189–227. https://doi.org/10.1039/b905604c.

(7) Martinić, I.; Eliseeva, S. V.; Nguyen, T. N.; Pecoraro, V. L.; Petoud, S. Near-Infrared Optical Imaging of Necrotic Cells by Photostable Lanthanide-Based Metallacrowns. *J. Am. Chem. Soc.* **2017**, *139* (25), 8388–8391. https://doi.org/10.1021/jacs.7b01587.

(8) Nguyen, T. N.; Chow, C. Y.; Eliseeva, S. V.; Trivedi, E. R.; Kampf, J. W.; Martinić, I.; Petoud, S.; Pecoraro, V. L. One-Step Assembly of Visible and Near-Infrared Emitting Metallacrown Dimers Using a Bifunctional Linker. *Chem. Eur. J.* **2018**, *24* (5), 1031–1035. https://doi.org/10.1002/chem.201703911.

(9) Chow, C. Y.; Eliseeva, S. V.; Trivedi, E. R.; Nguyen, T. N.; Kampf, J. W.; Petoud, S.; Pecoraro, V. L. Ga 3+ /Ln 3+ Metallacrowns: A Promising Family of Highly Luminescent Lanthanide Complexes That Covers Visible and Near-Infrared Domains. *J. Am. Chem. Soc.* **2016**, *138* (15), 5100–5109. https://doi.org/10.1021/jacs.6b00984.

(10) Kielar, F.; Law, G. L.; New, E. J.; Parker, D. The Nature of the Sensitiser Substituent Determines Quenching Sensitivity and Protein Affinity and Influences the Design of Emissive Lanthanide Complexes as Optical Probes for Intracellular Use. *Org. Biomol.*

Chem. **2008**, *6* (13), 2256–2258. https://doi.org/10.1039/b804369h.

(11) Mathieu, E.; Sipos, A.; Demeyere, E.; Phipps, D.; Sakaveli, D.; Borbas, K. E. Lanthanide-Based Tools for the Investigation of Cellular Environments. *Chem. Commun.* **2018**, *54* (72), 10021–10035. https://doi.org/10.1039/C8CC05271A.

(12) Pecoraro, V. L.; Stemmler, A. J.; Gibney, B. R.; Bodwin, J. J.; Wang, H.; Kampf, J. W.; Barwinski, A. Metallacrowns: A New Class of Molecular Recognition Agents. In *Progress in Inorganic Chemistry, Volume 45*; Wiley, 1997; pp 83–177. https://doi.org/10.1002/9780470166468.ch2.

(13) Chow, C. Y.; Trivedi, E. R.; Pecoraro, V.; Zaleski, C. M. Heterometallic Mixed 3d-4f Metallacrowns: Structural Versatility, Luminescence, and Molecular Magnetism. *Comments Inorg. Chem.* **2015**, *35* (4), 214–253. https://doi.org/10.1080/02603594.2014.981811.

(14) Ostrowska, M.; Fritsky, I. O.; Gumienna-Kontecka, E.; Pavlishchuk, A. V. Metallacrown-Based Compounds: Applications in Catalysis, Luminescence, Molecular Magnetism, and Adsorption. *Coord. Chem. Rev.* **2016**, *327–328*, 304–332. https://doi.org/10.1016/j.ccr.2016.04.017.

(15) Lah, M. S.; Pecoraro, V. L. Development of Metallacrown Ethers: A New Class of Metal Clusters. *Comments Inorg. Chem.* **1990**, *11* (2–3), 59–84. https://doi.org/10.1080/02603599008035819.

(16) Martinić, I.; Eliseeva, S. V.; Nguyen, T. N.; Foucher, F.; Gosset, D.; Westall, F.; Pecoraro, V. L.; Petoud, S. Near-Infrared Luminescent Metallacrowns for Combined: In Vitro Cell Fixation and Counter Staining. *Chem. Sci.* **2017**, *8* (9), 6042–6050. https://doi.org/10.1039/c7sc01872j.

(17) Azar, M. R.; Boron, T. T.; Lutter, J. C.; Daly, C. I.; Zegalia, K. A.; Nimthong, R.; Ferrence, G. M.; Zeller, M.; Kampf, J. W.; Pecoraro, V. L.; Zaleski, C. M. Controllable Formation of Heterotrimetallic Coordination Compounds: Systematically Incorporating Lanthanide and Alkali Metal Ions into the Manganese 12-Metallacrown-4 Framework. *Inorg. Chem.* **2014**, *53* (3), 1729–1742. https://doi.org/10.1021/ic402865p.

(18) Boron, T. T.; Lutter, J. C.; Daly, C. I.; Chow, C. Y.; Davis, A. H.; Nimthong-Roldán, A.; Zeller, M.; Kampf, J. W.; Zaleski, C. M.; Pecoraro, V. L. The Nature of the Bridging Anion Controls the Single-Molecule Magnetic Properties of DyX4M 12-Metallacrown-4 Complexes. *Inorg. Chem.* **2016**, *55* (20), 10597–10607.

https://doi.org/10.1021/acs.inorgchem.6b01832.

(19) Bari, L. Di; Pintacuda, G.; Salvadori, P.; Dickins, R. S.; Parker, D. Effect of Axial Ligation on the Magnetic and Electronic Properties of Lanthanide Complexes of Octadentate Ligands. *J. Am. Chem. Soc.* **2000**, *122* (38), 9257–9264. https://doi.org/10.1021/ja0012568.

(20) Fernández-Fernández, M. del C.; Bastida, R.; Macías, A.; Pérez-Lourido, P.; Platas-Iglesias, C.; Valencia, L. Lanthanide(III) Complexes with a Tetrapyridine Pendant-Armed Macrocyclic Ligand: 1 H NMR Structural Determination in Solution, X-Ray Diffraction, and Density-Functional Theory Calculations. *Inorg. Chem.* **2006**, *45* (11), 4484–4496. https://doi.org/10.1021/ic0603508.

(21) Valencia, L.; Martinez, J.; Macías, A.; Bastida, R.; Carvalho, R. A.; Geraldes, C. F. G. C. X-Ray Diffraction and 1 H NMR in Solution: Structural Determination of Lanthanide Complexes of a Py 2 N 6 Ac 4 Ligand. *Inorg. Chem.* **2002**, *41* (20), 5300–5312. https://doi.org/10.1021/ic0257017.

(22) Di Bari, L.; Lelli, M.; Pintacuda, G.; Pescitelli, G.; Marchetti, F.; Salvadori, P. Solution versus Solid-State Structure of Ytterbium Heterobimetallic Catalysts. *J. Am. Chem. Soc.* **2003**, *125* (18), 5549–5558. https://doi.org/10.1021/ja0297640.

(23) Di Bari, L.; Di Pietro, S.; Pescitelli, G.; Tur, F.; Mansilla, J.; Saá, J. M. [LnACHTUNGTRENUNG(Binolam)3]•(OTf)3, a New Class of Propeller-Shaped Lanthanide(III) Salt Complexes as Enantioselective Catalysts: Structure, Dynamics and Mechanistic Insight. *Chem. Eur. J.* **2010**, *16* (47), 14190–14201. https://doi.org/10.1002/chem.201001683.

(24) Bleaney, B. Nuclear Magnetic Resonance Shifts in Solution Due to Lanthanide Ions. *J. Magn. Reson.* **1972**, *8* (1), 91–100. https://doi.org/10.1016/0022-2364(72)90027-3.

(25) Rigault, S.; Piguet, C. Predictions and Assignments of NMR Spectra for Strongly Paramagnetic Supramolecular Lanthanide Complexes: The Effect of the "Gadolinium Break." *J. Am. Chem. Soc.* **2000**, *122* (38), 9304–9305. https://doi.org/10.1021/ja000958u.

(26) Ouali, N.; Rivera, J.-P.; Morgantini, P.-Y.; Weber, J.; Piguet, C. The Solution Structure of Homotrimetallic Lanthanide Helicates Investigated with Novel Model-Free Multi-Centre Paramagnetic NMR MethodsElectronic Supplementary Information (ESI) Available: Tables of Structural Factors Cikl, Dikl Obtained for the Model Com. *Dalton Trans.* **2003**, *3* (7), 1251–1263. https://doi.org/10.1039/b212352e.

(27) Di Pietro, S.; Piano, S. Lo; Di Bari, L. Pseudocontact Shifts in Lanthanide Complexes with

Variable Crystal Field Parameters. *Coord. Chem. Rev.* **2011**, *255* (23–24), 2810–2820. https://doi.org/10.1016/j.ccr.2011.05.010.

(28) Atzeri, C.; Marzaroli, V.; Quaretti, M.; Travis, J. R.; Di Bari, L.; Zaleski, C. M.; Tegoni, M. Elucidation of 1 H NMR Paramagnetic Features of Heterotrimetallic Lanthanide(III)/Manganese(III) 12-MC-4 Complexes. *Inorg. Chem.* **2017**, *56* (14), 8257–8269. https://doi.org/10.1021/acs.inorgchem.7b00970.

(29) Reilley, C. N.; Good, B. W.; Desreux, J. F. Structure-Independent Method for Dissecting Contact and Dipolar NMR Shifts in Lanthanide Complexes and Its Use in Structure Determination. *Anal. Chem.* **1975**, *47* (13), 2110–2116. https://doi.org/10.1021/ac60363a011.

(30) J -C G Bunzli, E. by V. K. P. *Handbook on the Physics and Chemistry of Rare Earths*; 2013. https://doi.org/10.1017/CBO9781107415324.004.

(31) Melegari, M.; Tegoni, M. Aspects of NMR Characterization of Metallacrowns. In *Advances in Metallacrown Chemistry*; Zaleski, C. M., Ed.; Springer International Publishing: Cham, 2022; pp 37–76. https://doi.org/10.1007/978-3-031-08576-5_2.

(32) Berbenni, V.; Milanese, C.; Bruni, G.; Marini, A. Thermal Decomposition of Gallium

Nitrate Hydrate Ga(NO3)3×xH2O. *J. Therm. Anal. Calorim.* **2005**, *82* (2), 401–407. https://doi.org/10.1007/s10973-005-0909-x.

(33) Bruker AXS Inc., Madison, Wisconsin, U. Bruker (2012). SMART. **2012**.

(34) Krause, L., Herbst-Irmer, R., S. G. M. & S. D. Bruker (2001). Program Name. Bruker AXS Inc., Madison, Wisconsin, USA. *J. Appl. Cryst. 48 3-10* **2001**.

(35) Sheldrick, G. M. SHELXT - Integrated Space-Group and Crystal-Structure Determination. *Acta Crystallogr. Sect. A Found. Crystallogr.* **2015**, *71* (1), 3–8. https://doi.org/10.1107/S2053273314026370.

(36) Sheldrick, G. M. Crystal Structure Refinement with SHELXL. *Acta Crystallogr. Sect. C Struct. Chem.* **2015**, *71* (Md), 3–8. https://doi.org/10.1107/S2053229614024218.

(37) Dolomanov, O. V.; Bourhis, L. J.; Gildea, R. J.; Howard, J. A. K.; Puschmann, H. OLEX2: A Complete Structure Solution, Refinement and Analysis Program. *J. Appl. Crystallogr.* **2009**, *42* (2), 339–341. https://doi.org/10.1107/S0021889808042726.

(38) Macrae, C. F.; Bruno, I. J.; Chisholm, J. A.; Edgington, P. R.; McCabe, P.; Pidcock, E.; Rodriguez-Monge, L.; Taylor, R.; Van De Streek, J.; Wood, P. A. Mercury CSD 2.0 - New Features for the Visualization and Investigation of Crystal Structures. *J. Appl. Crystallogr.*

2008, *41* (2), 466–470. https://doi.org/10.1107/S0021889807067908.

(39) Spek, A. L. PLATON SQUEEZE: A Tool for the Calculation of the Disordered Solvent Contribution to the Calculated Structure Factors. *Acta Crystallogr. Sect. C Struct. Chem.* 2015, *71*, 9–18. https://doi.org/10.1107/S2053229614024929.

(40) Willcott, M. R. MestRe Nova. *J. Am. Chem. Soc.* 2009, *131* (36), 13180–13180. https://doi.org/10.1021/ja906709t.

(41) Stevenson, K. J. Review of Originpro 8.5. *J. Am. Chem. Soc.* 2011, *133* (14), 5621. https://doi.org/10.1021/ja202216h.

(42) M. J. Frisch, G. W. Trucks, H. B. Schlegel, G. E. Scuseria, M. A. Robb, J. R. Cheeseman, G. Scalmani, V. Barone, G. A. Petersson, H. Nakatsuji, X. Li, M. Caricato, A. V. Marenich, J. Bloino, B. G. Janesko, R. Gomperts, B. Mennucci, H. P. Hratchian, J. V. Gaussian 16 Revision B.01. 2016.

(43) Guo, X. G.; Sun, H.; Sun, X. Structure, Bonding, and Electronic Properties of Four Rare Earth Complexes with a Phenoxyacetic Acid Ligand: X-Ray Diffraction and DFT Studies. *Ind. Eng. Chem. Res.* 2016, *55* (23), 6716–6722. https://doi.org/10.1021/acs.iecr.6b01077.

(44) Mardirossian, N.; Head-Gordon, M. How Accurate Are the Minnesota Density Functionals

for Noncovalent Interactions, Isomerization Energies, Thermochemistry, and Barrier Heights Involving Molecules Composed of Main-Group Elements? *J. Chem. Theory Comput.* **2016**, *12* (9), 4303–4325. https://doi.org/10.1021/acs.jctc.6b00637.

(45) Roca-Sabio, A.; Regueiro-Figueroa, M.; Esteban-Gómez, D.; de Blas, A.; Rodríguez-Blas, T.; Platas-Iglesias, C. Density Functional Dependence of Molecular Geometries in Lanthanide(III) Complexes Relevant to Bioanalytical and Biomedical Applications. *Comput. Theor. Chem.* **2012**, *999* (Iii), 93–104. https://doi.org/10.1016/j.comptc.2012.08.020.

(46) Grimme, S. Semiempirical GGA-Type Density Functional Constructed with a Long-Range Dispersion Correction. *J. Comput. Chem.* **2006**, *27* (15), 1787–1799. https://doi.org/10.1002/jcc.20495.

(47) Gordon, M. S.; Binkley, J. S.; Pople, J. A.; Pietro, W. J.; Hehre, W. J. Self-Consistent Molecular-Orbital Methods. 22. Small Split-Valence Basis Sets for Second-Row Elements. *J. Am. Chem. Soc.* **1982**, *104* (10), 2797–2803. https://doi.org/10.1021/ja00374a017.

(48) Cao, X.; Dolg, M. Segmented Contraction Scheme for Small-Core Actinide Pseudopotential Basis Sets. *J. Mol. Struct. THEOCHEM* **2004**, *673* (1–3), 203–209.

https://doi.org/10.1016/j.theochem.2003.12.015.

(49) Travis, J. R.; Smihosky, A. M.; Kauffman, A. C.; Ramstrom, S. E.; Lewis, A. J.; Nagy, S. G.; Rheam, R. E.; Zeller, M.; Zaleski, C. M. Syntheses and Crystal Structures of Two Classes of Aluminum-Lanthanide-Sodium Heterotrimetallic 12-Metallacrown-4 Compounds: Individual Molecules and Dimers of Metallacrowns. *J. Chem. Crystallogr.* **2021**, *51* (3), 372–393. https://doi.org/10.1007/s10870-020-00861-2.

(50) Parac-Vogt, T. N.; Pacco, A.; Nockemann, P.; Yuan, Y. F.; Görller-Walrand, C.; Binnemans, K. Mandelohydroxamic Acid as Ligand for Copper(II) 15-Metallacrown-5 Lanthanide(III) and Copper(II) 15-Metallacrown-5 Uranyl Complexes. *Eur. J. Inorg. Chem.* **2006**, No. 7, 1466–1474. https://doi.org/10.1002/ejic.200501015.

(51) Delville, A.; Stover, H. D. H.; Detellier, C. Crown Ether-Cation Decomplexation Mechanics. Sodium-23 NMR Studies of the Sodium Cation Complexes with Dibenzo-24-Crown-8 and Dibenzo-18-Crown-6 in Nitromethane and Acetonitrile. *J. Am. Chem. Soc.* **1987**, *109* (24), 7293–7301. https://doi.org/10.1021/ja00258a008.

(52) Lin, J. D.; Popov, A. I. Nuclear Magnetic Resonance Studies of Some Sodium Ion Complexes with Crown Ethers and [2]-Cryptands in Various Solvents. *J. Am. Chem. Soc.*

1981, *103* (13), 3773–3777. https://doi.org/10.1021/ja00403a026.

(53) Shamsipur, M.; Popov, A. I. Multinuclear NMR Study of Dibenzo-30-Crown-10 Complexes with Sodium, Potassium, and Cesium Ions in Nonaqueous Solvents. *J. Am. Chem. Soc.* **1979**, *101* (15), 4051–4055. https://doi.org/10.1021/ja00509a005.

(54) Colpas, G. J.; Hamstra, B. J.; Kampf, J. W.; Pecoraro, V. L. Preparation of VO3+ and VO2+ Complexes Using Hydrolytically Stable, Asymmetric Ligands Derived from Schiff Base Precursors. *Inorg. Chem.* **1994**, *33* (21), 4669–4675. https://doi.org/10.1021/ic00099a017.

(55) Bleaney, B.; Dobson, C. M.; Levine, B. A.; Martin, R. B.; Williams, R. J. P.; Xavier, A. V. Origin of Lanthanide Nuclear Magnetic Resonance Shifts and Their Uses. *J. Chem. Soc. Chem. Commun.* **1972**, No. 13, 791b. https://doi.org/10.1039/c3972000791b.

(56) Jaoul, A.; Nocton, G.; Clavaguéra, C. Assessment of Density Functionals for Computing Thermodynamic Properties of Lanthanide Complexes. *ChemPhysChem* **2017**, *18* (19), 2688–2696. https://doi.org/10.1002/cphc.201700629.

(57) Wang, J.; Lu, G.; Liu, Y.; Wu, S. G.; Huang, G. Z.; Liu, J. L.; Tong, M. L. Building Block and Directional Bonding Approaches for the Synthesis of {DyMn 4 } n (n = 2, 3) Metallacrown Assemblies. *Cryst. Growth Des.* **2019**, *19* (3), 1896–1902.

https://doi.org/10.1021/acs.cgd.8b01879.

(58) Nguyen, T. N.; Chow, C. Y.; Eliseeva, S. V.; Trivedi, E. R.; Kampf, J. W.; Martinić, I.; Petoud, S.; Pecoraro, V. L. One-Step Assembly of Visible and Near-Infrared Emitting Metallacrown Dimers Using a Bifunctional Linker. *Chem. – A Eur. J.* **2018**, *24* (5), 1031–1035. https://doi.org/10.1002/chem.201703911.

(59) Eliseeva, S. V.; Salerno, E. V.; Lopez Bermudez, B. A.; Petoud, S.; Pecoraro, V. L. Dy3+White Light Emission Can Be Finely Controlled by Tuning the First Coordination Sphere of Ga3+/Dy3+Metallacrown Complexes. *J. Am. Chem. Soc.* **2020**, *142* (38), 16173–16176. https://doi.org/10.1021/jacs.0c07198.

† The spectrum of Gd^{III}-1 was recorded but as expected, no peaks of the MC complex were detected due to the extremely short ^1H relaxation times induced by the Gd^{III} ion, and only a very broad band was present, approximately from 6 to 9 ppm, apart from those of the solvents. That is again different from what was observed for $Gd^{III}Na^{I}(OAc)_4[12\text{-}MC_{Mn^{III}(N)Shi}\text{-}4](H_2O)_4\cdot 6DMF$ in which the presence of five coupled paramagnetic centers resulted in faster electron relaxation rates for Gd^{III} and, therefore, observable NMR signals.

‡ The ⟨…⟩ brackets mean that the ⟨G(*i*)⟩ parameter was calculated by averaging those of the same i positions considering non-symmetry equivalent positions or the presence of disorder and consequent fractional occupancies

SYNOPSIS The structure in solution of a series of lanthanide metallacrowns were studied through paramagnetic ^{1}H NMR and DFT models. The analysis of NMR data (treated with the "all-lanthanide" method), X-ray structures and DFT models allowed to establish the nature of dynamic equilibrium processes in solution otherwise not noticeable form the X-ray data alone.

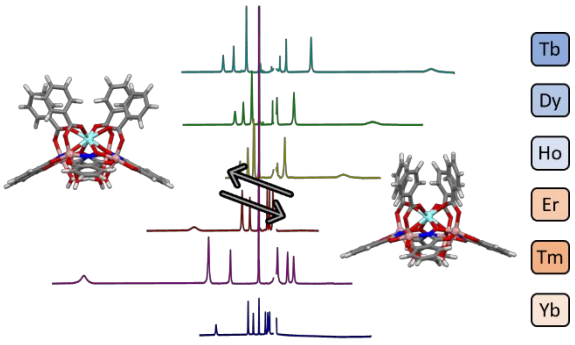

For Table of Contents Only